Mon. Not. R. Astron. Soc. **340,** 1153–1172 (2003)

Three-dimensional photoionization modelling of the planetary nebula NGC 3918

B. Ercolano,[1]★ C. Morisset,[2]† M. J. Barlow,[1] P. J. Storey[1] and X.-W. Liu[1]‡

[1] *University College London, Gower Street, London WC1E 6BT*
[2] *Laboratoire d'Astrophysique de Marseille, CNRS, BP 8, 13376 Marseille Cedex 12, France*

Accepted 2002 December 16. Received 2002 November 22; in original form 2002 September 20

ABSTRACT

The three-dimensional Monte Carlo photoionization code MOCASSIN has been applied to construct a realistic model of the planetary nebula NGC 3918. Three different geometric models were tried, the first being the biconical density distribution already used some years ago by Clegg et al. In this model the nebula is approximated by a biconical structure of enhanced density, embedded in a lower-density spherical region. Spindle-like density distributions were used for the other two models (models A and B). Model A used a mass distribution slightly modified from one of Mellema's hydrodynamical models that had already been adopted by Corradi et al. for their observational analysis of NGC 3918. Our spindle-like model B instead used an analytical expression to describe the shape of the inner shell of this object as consisting of an ellipsoid embedded in a sphere.

The effects of the interaction of the diffuse fields coming from two adjacent regions of different densities were investigated. These are found to be non-negligible, even for the relatively uncomplicated case of a biconical geometry. We found that the ionization structure of low-ionization species near the boundaries is particularly affected.

It is found that all three models provided acceptable matches to the integrated nebular optical and ultraviolet spectrum. Large discrepancies were found between all of the model predictions of infrared fine-structure line fluxes and *ISO* SWS measurements. This was found to be largely due to an offset of $\approx$14 arcsec from the centre of the nebula that affected all of the *ISO* observations of NGC 3918.

For each model, we also produced projected emission-line maps and position–velocity diagrams from synthetic long-slit spectra, which could be compared to recent *HST* images and ground-based long-slit echelle spectra. This comparison showed that spindle-like model B provided the best match to the observations. Although the integrated emission-line spectrum of NGC 3918 can be reproduced by all three of the three-dimensional models investigated in this work, the capability of creating projected emission-line maps and position–velocity diagrams from synthetic long-slit spectra was found to be crucial in allowing us to constrain the structure of this object.

Key words: ISM: abundances – planetary nebulae: individual: NGC 3918.

1 INTRODUCTION

The southern planetary nebula NGC 3918 (PN G294.6 + 04.7) is a very well known and widely studied object. A detailed study, based on ultraviolet (UV), optical and radio observations, was presented by Clegg et al. (1987, hereafter C87). The morphological and kinematical information available at the time of their work was, however, very limited, and, based on this, they constructed a photoionization model, using the Harrington code (e.g. Harrington et al. 1982), assuming a biconical geometry for a nebula seen almost *pole-on*. A two-dimensional representation of their model is shown in fig. 10 of C87. They had first tried a spherical model, deriving the radial hydrogen density distribution from the average radial intensity profile in the Hβ map they used, which had been obtained at the Boyden

★E-mail: be@star.ucl.ac.uk
†Present address: Instituto de Astronomia, Universidad Nacional Autónoma de México, México, D.F. 04510, México.
‡Present address: Department of Astronomy, Peking University, Beijing 100871, China.

Observatory, South Africa, in 1973 by K. Reay and S. P. Worswick. The Zanstra temperature they derived for the central star was 117 000 K, corresponding to a luminosity of 4900 $L_{\odot}$, for an adopted distance of 1.5 kpc. This model did not succeed in reproducing the linestrengths from some of the high-ionization species observed, such as, for example, Ne V, O V and O IV. They interpreted this as an indication that the nebula could be optically thin in some directions as seen from the star; this led to the formulation of a biconical model. The presence of an optically thin phase required an upward correction to the original Zanstra temperature and, in the final model, they adopted the ionizing spectrum described by a non-local thermodynamic equilibrium (non-LTE) model atmosphere for a central star having an effective temperature of 140 000 K, a surface gravity of $\log g = 6.5$ and a photospheric He/H = 0.10 by number. This model atmosphere was calculated by C87 using the program of Mihalas & Auer (1975). The resulting nebular model seemed to reproduce the main spectroscopic features observed.

Present observational data, such as, for example, images of NGC 3918 taken by the *HST* (see Fig. 8) and the echellograms obtained in several emission lines by Corradi et al. (1999, hereafter C99) (see Fig. 10), show, however, that a biconical model is inconsistent with the spatio-kinematical structure of this planetary nebula. C99 presented an analysis of optical images and high-resolution long-slit spectra of three planetary nebulae, including NGC 3918. They concluded that the large-scale structure of this object consists of a bright inner shell of roughly elliptical shape, from which two fainter protrusions extend in the polar directions, giving what was described in their paper as an overall spindle-like appearance. This inner shell, which has a size of 12×20 arcsec^2, measured along its major and minor axes, is surrounded by an elliptical shell with a diameter of 16 arcsec. From the images and from the long-slit spectra, they obtained the basic kinematical, geometrical and orientation parameters of the inner shell. They adopted a hydrodynamical model by Mellema (1996) to reproduce, at least qualitatively, the observations. The model that gave the best fit was one, from Mellema's set, which posits an initial mass distribution strongly enhanced in the equatorial region, with a density contrast between the equatorial and the polar regions as large as 10 (see Fig. 1). The effects of an expanding shock driven by a strong wind would give a spindle-like structure similar to the one observed in the inner shell of NGC 3918. C99 derived the inclination and the kinematical parameters of the inner shell by using the spatio-kinematical model of Solf & Ulrich (1985) (which was also used to obtain Hα position–velocity diagrams, as well as the shape of the inner shell) to match the observational data. Their final model still showed some deviation from the observations, particularly in the long-axis position–velocity plot, which they attributed to simplified assumptions in the spatio-kinematical model. Photoionization calculations, however, were not carried out in their work, and therefore no comparison with the observed spectrum was available to them.

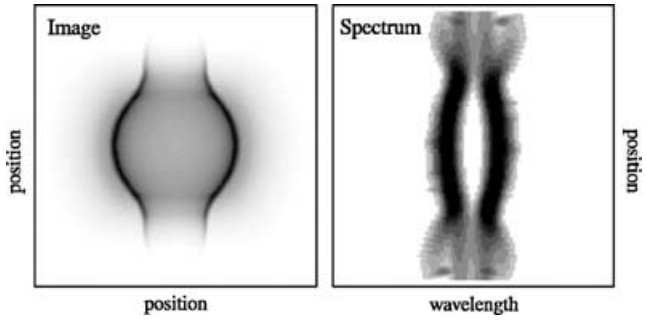

Figure 1. Model image (left) and long-axis synthetic slit spectrum (right) from the hydrodynamical models of Mellema (1996). Figure adapted by C99 from Mellema's original thesis work.

Given the large amount of observational data available for this object and the existence of the two different models described above, NGC 3918 seemed an excellent candidate for a detailed three-dimensional photoionization study using the MOCASSIN code described by Ercolano (2002) and (Ercolano et al. 2003, Paper I). Three photoionization models were constructed, using different density distribution descriptions, in order to try to reproduce the main spectroscopic features, as well as the projected maps published by C99. The models used a $23 \times 23 \times 23$ Cartesian grid, with the ionizing source being placed in a corner in order to utilize the symmetry of the geometries used. The complete model nebulae were, therefore, contained in $45 \times 45 \times 45$ cubic grids. All the grid cells have the same size. Velocity fields were then applied to the final converged grids in order to produce position–velocity diagrams to compare with the observations. In Section 2 the biconical density distribution model of C87 is described and the results obtained for it with MOCASSIN are presented and compared with those of C87, who used the one-dimensional Harrington code. A consistency test for the diffuse radiation field is also carried out in this section, in order to investigate the effects of discontinuities in the diffuse field transport in one-dimensional codes. The results obtained from the spindle-like models of NGC 3918 are presented in Section 3. Discrepancies were found between the predictions of all the models and the *ISO* SWS measurements of the infrared fine-structure lines; the possible reasons for these discrepancies are discussed in Section 4.

2 THE BICONICAL DENSITY DISTRIBUTION MODEL

The first nebular model to be run was the pole-on biconical distribution described by C87. This consisted of an optically thick biconical structure embedded into an optically thin sphere. The bicones are aligned along the polar axis of the nebula, which describes an angle of 15° with the line of sight. Exactly the same parameters were used for the central star and, apart from helium, argon and iron, the same nebular abundances as in their model; these are summarized in Table 1. The main reason for using exactly the same parameters is to be able to distinguish between the causes of any discrepancies between our model results and the original C87 model results. However, in the case of helium the empirical value derived by C87 was used instead of their model value, since it was commented in their paper that this is more reliable. In the case of argon and iron, their empirical abundances also had to be used, since these elements were

Table 1. Input parameters for the NGC 3918 biconical model.[a]

L_*	6900 $L_{\odot}$	He/H	0.107
$R_{\rm in}$	0.0 pc	C/H	8.0×10^{-4}
$R_{\rm out}$	0.106 pc	N/H	1.5×10^{-4}
$T_{\rm eff}$	140 000 K	O/H	5.0×10^{-4}
R_1	0.0333 pc	Ne/H	1.2×10^{-4}
n	2.3	Mg/H	1.4×10^{-5}
f	3	Si/H	1.0×10^{-5}
Φ	45°	S/H	1.6×10^{-5}
N_0	2381 cm^{-3}	Ar/H	2.0×10^{-6}
a/b	1	Fe/H	3.7×10^{-7}

[a]The abundances are given by number, relative to H.

not included in their code (that of J. P. Harrington) and, therefore, photoionization model results for them did not exist. The biconical radial density law that was adopted by C87, and which was mapped on to the three-dimensional Cartesian grid used in the current model, was constructed by them by deconvolving the observed nebular surface brightness, using the formalism of Harrington & Feibelman (1983), and has the form

$$N_{\rm H}(R) = N_0(R/R_1)^n \exp\left[-0.5(R/R_1)^2\right], \quad (1)$$

where $N_{\rm H}(R)$ is the hydrogen number density at distance R from the centre of the nebula, N_0 is a normalization constant, and R_1 and n are parameters which may be varied. The values used for these parameters are also given in Table 1, together with Φ, the half-angle of the density-enhanced cones, f, the density enhancement factor between the two regions, and a/b, the axial ratio. The optical depths at 1 Ryd (1 Ryd $= 2.180 \times 10^{-18}$ J), calculated at the outer edge of the nebula in the polar (optically thick) and equatorial (optically thin) directions, are 29.4 and 0.94, respectively.

2.1 The biconical density distribution model: results

Following the C87 analysis, emission-line fluxes are given relative to the total dereddened Hβ flux integrated over the entire nebula, on a scale where Hβ is equal to 100. The contributions from each sector and the total relative fluxes are listed in Table 2, together with C87's results for both sectors, and the total observed values. The last column of the table contains the references for the observational data used. The fractional ionic abundances were also calculated for the thin and the thick regions and are given in Table 4. The mean temperatures weighted by the ionic abundances are calculated and given in Table 5. The definitions for both the fractional ionic abundances, $f(N_{ij})$, and for the mean temperatures, $T(N_{ij})$, are given by Harrington et al. (1982) and are repeated here for convenience:

$$f(N_{ij}) = \frac{\langle N_{ij}\rangle}{\sum_k N_{ik}} \quad (2)$$

and

$$T(N_{ij}) = \frac{\int N_{\rm e} N_{ij} T_{\rm e}\, {\rm d}V}{\int N_{\rm e} N_{ij}\, {\rm d}V}, \quad (3)$$

where the average density of an ion over the nebular volume is defined as

$$\langle N_{ij}\rangle = \frac{\int N_{\rm e} N_{ij}\, {\rm d}V}{\int N_{\rm e}\, {\rm d}V}, \quad (4)$$

$N_{\rm e}$ and N_{ij} are the electron density and the density of ion j of element i, respectively, and the summation is over all k ionization stages; $T_{\rm e}$ is the electron temperature and dV is the volume element.

The fractional ionic abundances and the mean temperatures weighted by ionic species were also presented by C87 (their tables 18 and 19); these are of great use in this work as they provide important parameters for the comparison of the MOCASSIN model to that of C87. The observed value of the integrated Hβ flux was obtained from Cahn, Kaler & Stanghellini (1992) and it was dereddened by adopting an interstellar reddening constant, c(Hβ), equal to 0.40. This value, which is within the error bars of the value estimated by C87, $c({\rm H}\beta) = 0.43 \pm 0.05$, was derived by Tsamis et al. (2003) and has been adopted in this work because it was derived from observations of the optical Balmer emission lines, also published by Tsamis et al. (2003) and listed in our Table 2 (as reference 'a'). It was not necessary to adjust the infrared line fluxes as these are not affected significantly by interstellar reddening. The optical observations presented by Tsamis et al. (2003) were obtained by uniformly scanning a long slit across the nebula, a method which, when combined with the total Hβ flux measured using a large entrance aperture (e.g. Cahn et al. 1992), yields the total fluxes from the whole nebula for all emission lines detected in the optical spectrum. These fluxes can thus be directly compared to those measured with space-borne facilities using large apertures, such as the *IUE* in the ultraviolet and *ISO* in the infrared.

Most of the results shown in Table 2 are in reasonable agreement with the results published by C87, also reported in Table 2. For both models, however, the doubly ionized helium recombination line at 4686 Å is too strong, while the singly ionized helium triplet line at 5876 Å is too weak, when compared with the observations. This result is consistent with the ionic fractions listed in table 18 of C87 and in Table 4 of this work for these ions. It is worth noting, however, that the values of the relative fluxes that C87 observed for these lines are 45.0 for He II 4686 Å and 9.5 for He I 5876 Å, on a scale where Hβ = 100. These values are closer to their model values of 48.0 and 7.8 than are the more recent observations of 41.7 and 10.8 by Tsamis et al. (2003) quoted in Table 2, the former being the values they had tried to reproduce in their model. A better agreement with the more recent observations can be obtained by using a different model atmosphere for the ionizing source. As has already been mentioned, a non-LTE model atmosphere for a central star with an effective temperature of 140 000 K, log $g = 6.5$ and a photospheric He/H = 0.10 by number was used by C87 and here; however by increasing log g, the depth of the doubly ionized helium jump is increased. This will result in fewer He^+ ionizing photons and, therefore, lower He^{2+} and higher He^+ nebular ionic fractions. The values obtained by using a non-LTE model for a central star of the same luminosity, effective temperature and He/H ratio, but with log $g = 7.5$, are 9.2 and 48.0 for the He I 5876 Å and He II 4686 Å line fluxes (relative to Hβ, on a scale where Hβ = 100), respectively. These values are closer to the observations than those obtained with log $g = 6.5$ and reported in Table 2. One final point to be made about the nebular helium results is that, as was mentioned at the start of this section, the nebular helium abundance used in this work is the empirical value calculated by C87, He/H = 0.107 by number, which is slightly higher than the value they used in their model, He/H = 0.10; this also contributes to the difference between the results we obtained for the He II 4686 Å and He I 5876 Å line fluxes and those presented by C87.

Large discrepancies also exist between the two models' predictions and the *ISO* SWS fluxes measured by Bower (2001, reference 'd' in Table 2). This discrepancy is mainly due to a pointing error which affected all *ISO* observations of NGC 3918; this is discussed in more detail in Section 4 and Appendix C.

With regard to the other emission-line fluxes listed in Table 2, some discrepancies between the two models do exist, but they are, in the majority of cases, within 30 per cent and the overall ionization structure of the nebula coincides. In particular, large discrepancies were found between the current work and that of C87 in the predictions of the [Ne V] fine-structure line fluxes, which will be discussed in Appendix B. Considering the significant progress in atomic physics made in the past 15 years, on the one hand, and the completely different treatment of the radiative transfer adopted by the two codes, on the other, that there are some differences in the results obtained is hardly surprising. Neither the Opacity Project (Verner et al. 1996) nor the Iron Project (Hummer et al. 1993) existed in 1987 and the rates for other important processes have changed since then.

Table 2. Observed and predicted emission-line fluxes for NGC 3918 and predictions for the C87 biconical models.

Line	This work			Clegg et al.			Observed	Ref.[a]
	Thin	Thick	Total	Thin	Thick	Total		
$H\beta/10^{-10}$ erg cm^{-2} s^{-1}	0.45	1.88	2.33	0.45	1.86	2.32	2.29	b
$H\beta$ 4861	100	100	100	100	100	100	100	–
He I 5876	0.08	8.5	8.5	0.06	7.7	7.8	10.81	a
He II 4686	24	30	54	22	26	48	41.65	a
C II] 2326	0.21	57	57	0.72	81	82	31.24	a
C II 4267	0.004	0.32	0.32	0.006	0.32	0.32	0.50	a
[C II] 157.74 μm	0.0	0.35	0.35	–	–	–	0.21	c
C III] 1908	33	577	610	58.7	577	637	492.5	a
C III 4648	0.10	0.50	0.61	0.10	0.42	0.52	0.42	a
C III] 2297	1.11	5.9	7.0	1.0	4.9	5.9	5:	e
C IV 1550[b]	596	964	1560	659	779	1439	457.6	a
C IV 4658	0.25	0.16	0.40	0.24	0.16	0.40	0.33	a
[N I] 5199	0.0	0.21	0.21	–	–	–	0.63	a
[N II] 6584	0.06	73	73	0.2	73	73	84	a
[N III] 1751	2.0	22	24	4.6	25	29	26.7	a
[N III] 57.3 μm	0.64	12	13	1.0	12	13	13.5	c
N IV] 1486	19	26	45	31	26	57	46.4	a
N V 1240[b]	42	22	64	47	19	66	41.4	a
[O I] 6300	0.0	2.7	2.7	0.0	0.56	0.56	5.24	a
[O I] 63.12 μm	0.0	0.23	0.23	–	–	–	6.72	c
[O I] 145.5 μm	0.0	0.018	0.018	–	–	–	0.23	c
[O II] 3727	0.08	104	104	0.2	89	89	94.5	a
[O III] 51.8 μm	2.8	90	93	4.0	94	98	88.6	c
[O III] 88.4 μm	0.91	16	17	1.3	17	19	27.51	c
[O III] 5007	40	1543	1583	63	1539	1602	1657	a
[O III] 4363	0.85	19	20	1.4	18.9	20	21.6	a
[O IV] 25.9 μm	190	161	352	274	177	451	89	d
O IV] 1402	16	14	30	28	16	43	48.9	a
O IV 1342	1.4	0.83	2.2	1.0	0.6	1.6	2:	e
[Ne II] 12.8 μm	0.001	0.94	0.94	0.0	0.77	0.77	12:	f
[Ne III] 15.6 μm	1.8	130	132	1.3	167	168	46.3	d
[Ne III] 3869	4.1	161	165	3	172	175	135.5	a
[Ne IV] 2423	35	42	77	50	52	102	132	e
[Ne V] 3426	75	45	119	70	40	110	80	e
[Ne V] 14.3 μm	179	107	286	18	13	31	19.6	d
[Ne V] 24.3 μm	156	64	220	30	19	49	23.1	d
[Ne VI] 7.6 μm	49	22	70	11	4.9	15.8	–	–
Mg I] 4565	0.00	0.73	0.73	0.00	0.28	0.28	0.13	a
Mg II 2800[b]	0.26	78	78	0.01	43	43	$\leqslant$1	e
[Mg IV] 4.49 μm	0.42	3.1	3.5	0.96	4.4	5.4	–	–
[Mg V] 2783	2.2	2.4	4.6	3.2	2.6	5.8	5.6	e
[Mg V] 5.6 μm	4.5	6.3	10.9	4.9	5.4	10.3	–	–
Si III] 1887	0.97	15	16	1.2	12.5	13.7	8	e
Si IV 1399[b]	2.7	7.9	11	2.8	5.4	8.2	9	e
[S II] 4070	0.0	2.1	2.1	0.0	2.8	2.8	2.693	a
[S III] 18.7 μm	0.03	38	38	0.31	38	38	8.7	d
[S III] 33.6 μm	0.02	16	16	0.2	15.6	16	–	–
[S III] 6312	0.006	3.7	3.7	0.005	3.4	3.4	2.27	a
[S IV] 10.5 μm	7.23	207	214	24	210	234	35.0	d

[a]References: a, Tsamis et al. (2003); b, Cahn et al. (1992); c, Liu et al. (2001); d, Bower (2001); e, C87; f, Pottasch et al. (1986).
[b]Attenuated by dust absorption.

MOCASSIN's predictions for electron density and temperature diagnostic line ratios are compared to those obtained by C87 and to the observed ratios in Table 3. There is very good agreement between the two models' predictions of line ratios, which is to be expected, since the density distributions used were the same. The small differences observed are reflected in the predicted emission-line fluxes, listed in Table 2, and, as has already been discussed, can probably be mostly assigned to differences in the atomic data sets. The diffuse radiation field, however, might also have some effect on the ionization structure, especially at the edges between the two sectors and in the outer regions of the nebula.

2.1.1 Resonance lines

There are some large discrepancies between the predictions of both the MOCASSIN and C87 models and the observations for the fluxes

Table 3. Diagnostic ratios for the electron density, N_e, and electron temperature, T_e (MOCASSIN, C87 biconical model, and observed).

Ion[a]	Lines (Å)	Moc.	Ratio C87	Obs.	Obs. ref.[b]
N_e					
Mg I	4562/4571	0.54	0.42:	0.28	1
S II	6716/6731	0.72	0.70	0.57	1
O II	3726/3729	1.63	1.61	1.98	2
O II	7325/3727[c]	0.071	–	0.078	1
C III	1906/1909	1.34	1.36	1.31	2
Si III	1883/1892	1.28	1.30	1.37	2
Ne IV	2421/2424	0.94	0.93	1.00	2
N IV	1483/1486	1.50	1.87	1.85	2
O IV	1401/1404	1.21	1.14	1.50	2
T_e					
N II	5755/6584	0.022	0.025	0.021	1
S II	4073/6724[d]	0.17	–	0.34	1
C^{2+}	4267/1908	0.0005	0.0005	0.0008	2
S III	6312/9532	0.032	0.029	0.032	2
O III	4363/5007	0.013	0.013	0.013	1
Ne IV	1602/2423	0.049	0.049	0.047	2
Ne V	1575/3426	0.0104	0.012	0.007:	2

[a]In order of increasing ionization potential.
[b]References: 1, Tsamis et al. (2003); 2, Clegg et al. (1987).
[c](7321+7332)/(3726+3729).
[d](4068+4076)/(6717+6731).

of the C IV 1550 Å and Mg II 2800 Å resonance lines. The reason for this is that these lines are attenuated by nebular dust absorption, which was not accounted for in this work, or by C87. Moreover, Mg II 2800 Å also suffers from absorption by interstellar Mg^+ and this is probably the main reason for the almost total absence of this line in the observed spectrum. Resonance lines must travel a much longer effective distance to escape from a nebula than do forbidden lines or the continuum radiation, because of the high optical depth in them; this translates into an enhanced probability of absorption by dust. The N V 1240 Å resonance doublet is also affected by this process, although in a minor way. The Si IV resonance line doublet at 1393 and 1401 Å can also be subject to attenuation by dust absorption; however, this line appears to be only slightly overestimated by the MOCASSIN model and is in agreement with the observations in C87. Harrington, Monk & Clegg (1988) published a dust model for NGC 3918 which confirms that the intensities of the resonance lines are indeed reduced. In their dust model Harrington et al. followed the same method as in the C87 photoionization model for this object: treating the thin and the thick sectors as two separate, spherically symmetric objects and then combining the results, weighted by the respective volume of each sector, i.e. 29 per cent for the thick sector and 71 per cent for the thin sector. In their model they found that the total flux of the C IV 1550 Å doublet, relative to $H\beta = 100$, was reduced from 1435 to 950, with 45 per cent of photons destroyed in the optically thick sector and 21 per cent in the optically thin sector. Their attenuated flux was still 85 per cent too strong compared to the observed value that they used, $F(1550) = 512$, and 107 per cent too strong compared to the more recently recalibrated and extracted *IUE* archive spectra presented by Tsamis et al. (2003), $F(1550) = 458$. Harrington et al. (1988) did not give a final answer as to whether the cause of this discrepancy lies in the photoionization model producing too much C IV line radiation or in the dust model being too ineffective in destroying it. However, they speculate that, if the grain opacity near 1550 Å was greater in their dust model, more line photons would be destroyed, hence improving the fit. The flux of N V 1240 Å, relative to $H\beta = 100$, is reduced from 66 to 52, with 25 per cent of photons being destroyed in the thick sector and 20 per cent in the thin sector. The value measured by Tsamis et al. (2003) for this line is 41.4. In the case of Si IV 1400 Å, dust actually makes the fit worse, by attenuating the flux, relative to $H\beta = 100$, from 8.2 to 5.7, whereas the observed value is 9.0 (C87). This is, however, a weak line and the observed flux might not be accurate. Finally, Harrington et al. (1988) predicted that the flux of Mg II 2800 Å is also reduced by dust attenuation, from 43 to 29. However, as mentioned above, this line shows evidence of interstellar absorption, so it cannot be measured properly. Aside from this, the dusty photoionization model of Harrington et al. (1988) is nearly identical to the one presented by C87.

2.1.2 The ionization structure

The general ionization structures of the C87 biconical nebula calculated by the two codes, and shown in table 18 of C87 and in Table 4 of this work, are in satisfactory agreement, with small differences, which, again, can mainly be attributed to improvements in the atomic data and the different treatments of the radiative transfer. In fact, although both codes treat the diffuse field exactly, the C87 model could not allow for transfer of diffuse radiation between the thick and the thin sectors. As shown by the scatter of values obtained for the benchmark problems (Péquignot et al. 2001; Ercolano 2002; Ercolano et al. 2003), even amongst one-dimensional classical codes it is usual for different codes to return slightly different predictions for the same problem, even in the extremely simplified case of homogeneous, spherically symmetric nebulae. Fig. 2 shows plots of the ionization structure of oxygen (middle panels) and carbon (bottom panels) as a function of radius along the optically thin polar direction (left panels) and along the optically thick equatorial direction (right panels). The ionization structure of helium is also plotted in each panel. The electron density distribution is also plotted as a function of radius for the optically thin polar direction (top left panel) and for the optically thick equatorial direction (top right panel). The effects of the charge exchange reaction $O^{3+} + H^0 \rightarrow O^{2+} + H^+$ are evident, particularly in the optically thick region, where $f(He^{2+})$ is about 10 per cent larger than the sum of $f(O^{3+}) + f(O^{4+}) + f(O^{5+}) + \cdots$.

2.1.3 The temperature structure

The mean temperatures weighted by ionic species calculated by MOCASSIN for the C87 biconical model are listed in Table 5; these can be compared to those calculated by C87, as listed in table 19 of their paper. The most obvious difference between the two sets of results is that MOCASSIN's mean temperatures are systematically lower than Clegg et al.'s. This effect is even more pronounced for the optically thin region. First of all, the higher collision strengths for the [Ne V] fine-structure lines, as calculated by Aggarwal (1983) and by Lennon & Burke (1991), and used in this work (see Appendix B), will make [Ne V] an important coolant. Furthermore, the fact that in the optically thin region the fractional ionic abundance of Ne^{4+} is higher could also explain why this region seems to be more affected by the cooling. It is also worth noticing that the mean ionic temperatures predicted by C87 show very little variation for the neutral species in each sector. These temperatures are all concentrated around 12 065 ± 35 K for the neutral species in

Table 4. Nebular averaged fractional ionic abundances for NGC 3918 (MOCASSIN, C87 biconical model).[a]

Element	Ion						
	I	II	III	IV	V	VI	VII
H	0.14 (−1)	0.986					
	0.51 (−3)	0.999					
He	0.44 (−2)	0.671	0.325				
	0.95 (−5)	0.028	0.972				
C	0.12 (−3)	0.053	0.487	0.333	0.128		
	0.46 (−7)	0.21 (−3)	0.028	0.260	0.711		
N	0.15 (−2)	0.065	0.464	0.365	0.071	0.033	
	0.12 (−7)	0.12 (−3)	0.039	0.342	0.365	0.254	
O	0.80 (−2)	0.067	0.674	0.156	0.070	0.021	0.43 (−2)
	0.21 (−7)	0.83 (−4)	0.039	0.368	0.395	0.164	0.034
Ne	0.54 (−4)	0.11 (−1)	0.733	0.133	0.102	0.021	0.65 (−3)
	0.32 (−8)	0.55 (−4)	0.038	0.258	0.536	0.162	0.48 (−2)
S	0.17 (−4)	0.027	0.294	0.362	0.214	0.081	0.022
	0.30 (−9)	0.27 (−5)	0.84 (−3)	0.039	0.348	0.438	0.173
Si	0.21 (−3)	0.325	0.195	0.256	0.127	0.078	0.019
	0.14 (−6)	0.62 (−3)	0.015	0.092	0.322	0.425	0.144
Mg	0.32 (−2)	0.112	0.532	0.119	0.118	0.098	0.018
	0.61 (−6)	0.59 (−4)	0.34 (−2)	0.056	0.298	0.507	0.136

[a]For each element the upper row is for the optically thick phase and the lower row is for the optically thin phase.

the optically thick sector, and around 16 120 ± 210 K for the optically thin sector [if $T_e(H^0) = 16$, 330 K is excluded, then the rest of the neutral ion temperatures in the optically thin sector are grouped around the value 16 005 ± 95 K]. The scatter gets larger for the higher ionization species. MOCASSIN's results, on the other hand, show a larger scatter, even for the mean temperatures of the neutral species, with their temperatures grouped around 10 960 ± 896 K for the optically thick region and 15 105 ± 682 K for the optically thin region. One probable explanation for this effect is the fact that, in C87's work, the biconical geometry is reproduced by combining two separate spherically symmetric models, hence taking no account of the interaction between the diffuse fields from the two phases, which could lead to fluctuations in local temperatures, particularly at the boundaries between the two regions. This is discussed in more detail in the next subsection.

2.2 Diffuse radiation field consistency test

C87 combined two appropriately weighted, spherically symmetric models to reproduce the biconical geometry. A consequence of this approach was that the diffuse radiation field was not treated self-consistently, especially near the boundaries of the two zones. The effects of the diffuse radiation field are expected to be small, but they could account for some of the differences between MOCASSIN's results and those obtained with the spherically symmetric Harrington code. In order to investigate the magnitude of these effects, the biconical distribution was modelled again using MOCASSIN, but this time each sector was treated as if it were spherically symmetric. The results from each sector were then weighted by the volume of the same sector and added together to yield the total flux relative to the total Hβ flux from the whole nebula. From now on this model will be referred to as the *composite model*.

Table 6 lists the fluxes of the emission lines relative to Hβ, on a scale where Hβ is equal to 100, for each sector. For ease of comparison, the results from the previous, self-consistent model are also given in the same table. Tables 7 and 8 list the fractional ionic abundances and the weighted mean electron temperatures for individual ionic species for the composite model. It becomes apparent from inspection of Table 6 that all of the collisional lines coming from lower ionization species are much weaker in the optically thick region of the composite model than in the same region of the self-consistent model. This is consistent with the fractional ionic abundances of low-ionization species being lower in the optically thick region of the composite model (Table 8), hence yielding lower line fluxes. The helium recombination line intensities calculated for the optically thick region of the composite model also indicate a lower abundance of He^0 and He^{2+}, but a higher He^+ abundance, which is confirmed by the results in Table 7. The optically thin region results do not seem to be affected as much and they are almost identical for the composite and for the self-consistent model. There are two main causes for the discrepancies observed between the results for the optically thick regions of the composite and self-consistent models. First of all, the diffuse radiation field coming from the optically thin region of the self-consistent model is weaker than the diffuse field coming from the same region in the optically thick spherically symmetric nebula of the composite model, since the diffuse field is approximately proportional to the square of the density and the densities in the two regions of the spherically symmetric optically thick composite model are, obviously, the same and are higher than the density in the optically thin region of the self-consistent model. This means that more diffuse photons are available to ionize the low-ionization-potential species in the composite model than there are in the self-consistent one. Secondly, the shape of the diffuse continuum at the edges between the two regions is different in the two models. In the self-consistent model the diffuse photons coming from the optically thin region will have higher frequencies, on average, than those coming from the same region in the optically thick spherically symmetric nebula of the composite model; this is due to the fact that in the optically thin medium the gas is in a higher ionization state. The photoionization cross-sections of the lower ionization species in the optically thick region of the self-consistent model will be, in general, quite small at the higher frequencies typical of the diffuse photons coming from the optically thin region and so these species will be less efficiently ionized by them. In the composite model, however, since the density distribution is spherically symmetric, the ionization structure is also the same in all radial directions; this

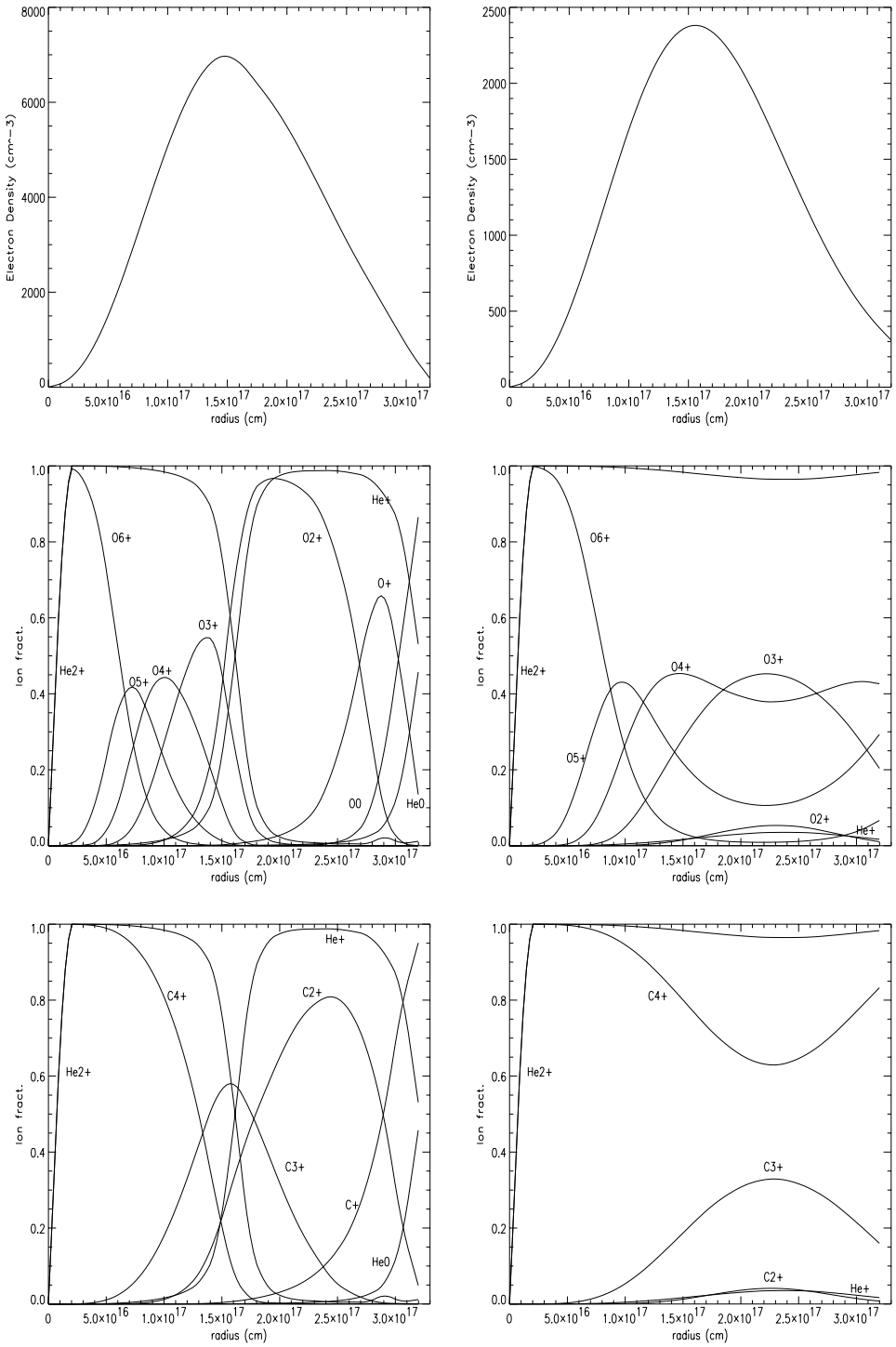

Figure 2. MOCASSIN ionic fractions for oxygen (middle panels) and carbon (bottom panels) along the polar (left panels) and equatorial (right panels) directions for the C87 biconical model for NGC 3918. The ionization structure of helium is also plotted in each panel. The top panels show the electron density plotted as a function of radius along the polar (top left) and equatorial (top right) directions.

means that the diffuse photons coming from adjacent regions will have frequencies close to the ionization thresholds of the lower ionization species, which will, therefore, be ionized to a greater degree than in the self-consistent model. On the other hand, the optically thin region of the self-consistent model will not be affected by the lower energy diffuse photons coming from the optically thick region since the gas in the optically thin region is already in a higher ionization stage. The combination of the two effects discussed above explains why the abundances of lower ionization species are lower in the optically thick region of the composite model than in the same region of the self-consistent one.

Another striking feature that emerges from running the composite spherically symmetric model is in the prediction of mean temperatures weighted by ionic species shown in Table 8. As mentioned

Table 5. Mean temperatures (K) weighted by ionic species for NGC 3918 (MOCASSIN, C87 biconical model).[a]

Element	Ion						
	I	II	III	IV	V	VI	VII
H	11 386	12 925					
	15 881	16 326					
He	11 247	12 044	14 703				
	15 495	15 722	16 344				
C	11 582	11 585	12 116	13 133	15 858		
	15 300	15 459	15 603	15 861	16 526		
N	10 339	11 522	12 182	13 186	15 435	17 312	
	15 348	15 506	15 631	15 842	16 234	17 217	
O	10 834	11 618	12 221	14 507	15 680	17 081	20 296
	14 874	15 298	15 509	15 887	16 260	17 020	19 477
Ne	10 136	11 636	12 156	14 340	15 561	17 360	22 911
	14 990	15 243	15 467	15 859	16 269	17 301	21 769
S	11 549	11 412	11 845	12 409	13 887	15 584	17 637
	15 016	15 115	15 353	15 603	15 910	16 285	17 437
Si	11 817	11 794	12 349	12 875	14 333	15 543	17 684
	15 362	15 398	15 561	15 677	15 949	16 364	17 563
Mg	11 747	11 690	12 013	13 491	14 605	15 547	17 563
	14 517	15 530	14 963	15 632	15 919	16 329	17 526

[a]For each element the upper row is for the optically thick phase and the lower row is for the optically thin phase.

in the previous subsection, the mean ionic temperatures predicted by C87 show very little variation amongst the neutral species in each sector, whereas the scatter of the results from MOCASSIN's self-consistent model is much larger. It was anticipated that a possible explanation for this effect could be the fact that in Clegg et al.'s work the diffuse radiation field transfer was not self-consistent, particularly near the boundaries between the two density regions, and that the interaction between the diffuse radiation fields of the two phases could lead to the fluctuations in the kinetic temperatures obtained in MOCASSIN's self-consistent model. The results obtained from MOCASSIN's composite model indeed confirm this hypothesis – within each sector the fluctuations in the mean ionic temperatures weighted by ionic abundances for neutral species disappear and their distribution resembles that obtained by C87 although the MOCASSIN temperatures are still slightly lower, particularly in the thin sector.

In conclusion, it is clear that the effects of the diffuse radiation field near the boundaries between the two phases are not negligible, even for the simple biconical distribution used in this case. These effects are particularly important for the abundances of the lower ionization species. It is not clear, however, why the ionization structure calculated by C87 (their table 18), who used a composite model, bears more resemblance to MOCASSIN's self-consistent model results (see Table 4), than to MOCASSIN's composite model results (see Table 7). Unfortunately, owing to the completely different approach to the radiative transfer used by the two codes and the fact that 15 years have passed since C87's work, over which period the atomic data base has evolved considerably, any further comparison between the two codes becomes difficult.

3 A SPINDLE-LIKE DENSITY DISTRIBUTION MODEL FOR NGC 3918

Fig. 1, from C99, shows a qualitative representation of a density distribution obtained from a hydrodynamical model by Mellema (1996) that was adopted by C99 in their observational study of the spatio-kinematical properties of NGC 3918. The model chosen was one from a set that Mellema (1996, page 126) computed for his original thesis work (parameters $B = 6$ and $A = 0.9$ in his calculations).

The exact density distribution for the model used in the C99 paper was kindly provided by Dr G. Mellema, and a first attempt to construct a photoionization model for this distribution was carried out. The density distribution, however, had to be scaled up by a factor of 1.6 in order to match the observed Hβ flux. However, the integrated emission-line spectrum still did not match the observations,

Table 6. Predicted emission-line fluxes for NGC 3918 (composite versus self-consistent model).

Line	Composite			Self-consistent		
	Thin	Thick	Total	Thin	Thick	Total
H $\beta/10^{-10}$ erg cm^{-2} s^{-1}	0.45	1.90	2.35	0.45	1.88	2.33
Hβ 4861	100	100	100	100	100	100
He I 5876	0.07	8.7	8.8	0.08	8.5	8.5
He II 4686	23	28	51	24	30	54
C II] 2326	0.22	34	34	0.21	57	57
C II 4267	0.004	0.31	0.31	0.004	0.32	0.32
[C II] 157.74 μm	0.0005	0.12	0.12	0.0	0.35	0.35
C III] 1908	33	551	584	33	577	610
C III 4648	0.10	0.56	0.66	0.10	0.50	0.61
C III] 2297	1.05	6.6	7.7	1.11	5.9	7.0
C IV 1550	607	968	1575	596	964	1560
C IV 4658	0.24	0.16	0.40	0.25	0.16	0.40
[N I] 5199	0.0	0.006	0.006	0.0	0.21	0.21
[N II] 6584	0.06	27	28	0.06	73	73
N III] 1751	2.0	22	22	2.0	22	24
[N III] 57.3 μm	0.60	14	15	0.64	12	13
N IV] 1486	19	26	45	19	26	45
N V 1240	44	21	65	42	22	64
[O I] 6300	0.0	0.18	0.18	0.0	2.7	2.7
[O I] 63.12 μm	0.0	0.011	0.012	0.0	0.23	0.23
[O I] 145.5 μm	0.0	0.0008	0.0008	0.0	0.018	0.018
[O II] 3727	0.08	47.5	48	0.08	104	104
[O III] 51.8 μm	2.4	101	103	2.8	90	93
[O III] 88.4 μm	0.75	19	20	0.91	16	17
[O III] 5007	35	1624	1659	40	1543	1583
[O III] 4363	0.78	20	21	0.85	20	20
[O IV] 25.9 μm	186	157	143	190	161	352
O IV] 1402	16	14	29	16	14	30
O IV 1342	1.3	0.84	2.1	1.4	0.83	2.2
[Ne II] 12.8 μm	0.001	0.62	0.64	0.001	0.94	0.94
[Ne III] 15.6 μm	1.6	130	133	1.8	130	132
[Ne III] 3869	3.7	161	165	4.1	161	165
[Ne IV] 2423	36	41	77	35	42	77
[Ne V] 3426	76	44	120	75	45	119
[Ne V] 14.3 μm	176	110	286	179	107	286
[Ne V] 24.3 μm	154	65	219	156	64	220
[Ne VI] 7.6 μm	49	21	70	49	22	70
Mg I] 4565	0.0	0.34	0.38	0.0	0.73	0.73
Mg II 2800	0.20	57	57	0.26	78	78
[Mg IV] 4.49 μm	0.39	3.1	3.5	0.42	3.1	3.5
[Mg V] 2783	2.2	2.4	4.6	2.2	2.4	4.6
[Mg V] 5.6 μm	4.4	6.6	11	4.5	6.3	11
Si III] 1887	1.1	14	15	0.97	15	16
Si IV 1399	2.9	7.6	11	2.7	7.9	11
[S II] 4070	0.0	1.3	1.3	0.0	2.1	2.1
[S III] 18.7 μm	0.03	32	32	0.03	38	38
[S III] 33.6 μm	0.020	14	14	0.02	16	16
[S III] 6312	0.006	3.2	3.2	0.006	3.7	3.7
[S IV] 10.5 μm	6.8	223	235	7.23	207	214

Table 7. Fractional ionic abundances for NGC 3918 (MOCASSIN, composite biconical model).[a]

Element	Ion						
	I	II	III	IV	V	VI	VII
H	0.61 (−2)	0.994					
	0.54 (−3)	0.999					
He	0.19 (−2)	0.697	0.301				
	0.88 (−5)	0.025	0.975				
C	0.61 (−4)	0.029	0.481	0.366	0.124		
	0.56 (−7)	0.20 (−3)	0.027	0.254	0.718		
N	0.97 (−4)	0.025	0.476	0.399	0.068	0.032	
	0.26 (−7)	0.12 (−3)	0.037	0.334	0.369	0.259	
O	0.49 (−3)	0.031	0.730	0.149	0.066	0.020	0.42 (−2)
	0.16 (−7)	0.72 (−4)	0.034	0.360	0.403	0.167	0.035
Ne	0.38 (−5)	0.76 (−2)	0.747	0.126	0.098	0.020	0.61 (−3)
	0.24 (−8)	0.45 (−4)	0.033	0.257	0.539	0.165	0.49 (−2)
S	0.32 (−5)	0.036	0.368	0.387	0.127	0.061	0.019
	0.16 (−7)	0.14 (−3)	0.015	0.126	0.275	0.413	0.170
Si	0.13 (−3)	0.268	0.207	0.282	0.143	0.080	0.019
	0.19 (−6)	0.66 (−3)	0.016	0.094	0.319	0.425	0.144
Mg	0.17 (−2)	0.082	0.638	0.133	0.066	0.065	0.014
	0.40 (−5)	0.34 (−3)	0.024	0.162	0.248	0.441	0.123

[a]For each element the upper row is for the optically thick phase and the lower row is for the optically thin phase.

Table 8. Mean temperatures (K) weighted by ionic species for NGC 3918 (MOCASSIN, composite biconical model).[a]

Element	Ion						
	I	II	III	IV	V	VI	VII
H	12 060	12 880					
	16 061	16 486					
He	11 965	12 052	14 770				
	15 844	16 001	16 498				
C	11 964	11 985	12 108	12 931	15 661		
	15 702	15 757	15 842	16 039	16 667		
N	12 022	12 002	12 147	12 992	15 279	17 065	
	15 704	15 761	15 842	16 006	16 369	17 360	
O	12 032	11 989	12 155	14 481	15 507	16 862	20 001
	15 678	15 749	15 838	16 036	16 388	17 153	19 615
Ne	11 958	11 990	12 146	14 301	15 394	17 122	22 502
	15 686	15 736	15 817	16 010	16 406	17 449	21 943
S	11 986	11 982	12 946	12 233	13 638	15 402	17 367
	15 675	15 689	15 742	15 850	16 075	16 419	17 573
Si	11 919	11 947	12 169	12 624	14 066	15 293	17 397
	15 674	15 704	15 773	15 858	16 100	16 518	17 744
Mg	11 919	11 929	11 957	13 408	14 490	15 372	17 322
	15 650	15 671	15 717	15 841	16 066	16 473	17 680

[a]For each element the upper row is for the optically thick phase and the lower row is for the optically thin phase.

as the emission-line strengths from the lower ionization species were heavily underestimated. From the images, however, it is evident that NGC 3918 has an inner shell of denser material that *screens* the gas behind it from direct starlight, thus allowing the existence of a lower ionization region. In Mellema's simulations such *shells* can only be made by considering an evolving central star and having a slow H ionization front. This, however, was not the case for the model used in C99 analysis. In order to simulate such a dense inner shell, the density was artificially raised in the equatorial region to form a thick torus between the two lobes. The torus had to be thick enough to screen the material behind it effectively, and the latitudinal extension of the density enhancement was determined such that the model would return the observed Hβ flux. This trade-off between the density enhancement factor and its spatial extension resulted in the creation of a thick equatorial waist. The three-dimensional isodensity plot (obtained for a high density threshold) of the final density distribution used for this model is shown in Fig. 3. This model will be referred to as *model A*.

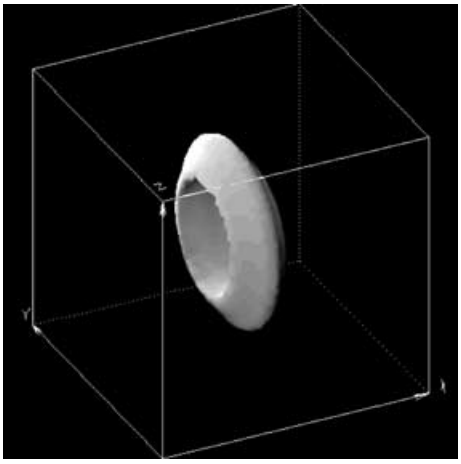

Figure 3. Three-dimensional isodensity plot of the dense torus component of spindle-like model A.

A second attempt to reconstruct the density distribution of this object was to seek an analytical expression that could reproduce the structure shown in Fig. 1 and in the *HST* and NTT images published by C99. The parameters of the central star and the adopted nebular abundances were the same as in the biconical model. The density distribution was obtained by combining a sphere with an ellipsoid, using a set of analytical expressions as described in Appendix A. The best fit to the observed integrated spectrum and to the images of NGC 3918 was obtained using the parameters listed in Table 9. Fig. 4 shows the three-dimensional isodensity plot corresponding to this combination. In this work the spindle-like model constructed by using the analytical description will be referred to as *model B*.

C99's study primarily focused on the kinematics of NGC 3918 and therefore they did not propose any new values for the central star parameters or for the nebular elemental abundances. Although derived for a different density distribution, the parameters derived by C87 were used by us for these models too. As given by C87, the dereddened stellar flux at 1300 Å is equal to 2.4×10^{-12} erg cm^{-2} s^{-1} Å^{-1}. For an assumed distance of 1.5 kpc and a stellar effective temperature of $T_{\rm eff} = 150\,000$ K, this flux corresponds to a stellar luminosity, L_*, of 5780 $L_\odot$.

The stellar luminosity in the C87 model, however, was finally adjusted by them to a slightly higher value of $F_*(1300\ \text{Å}) = 2.9 \times 10^{-12}$ erg cm^{-2} s^{-1} Å^{-1}, corresponding to $L_* = 6900\ L_\odot$. In this work both values for $F_*(1300$ Å) were used, in turn, for both

Table 9. Input shape and thickness parameters for the analytical fit to the density distribution of spindle-like model B (see Appendix A).

n_1 (cm^{-3})	18 000	$\Delta\theta$ (deg)	10
θ_1 (deg)	25	$\Delta r_{\rm eq}^{\rm in}$	0.06
$r_{\rm eq}$	0.3	$\Delta r_{\rm eq}^{\rm out}$	0.2
$r_{\rm po}$[a]	0.2	$\Delta r_{\rm po}^{\rm in}$	0.0032
e	0.25	$\Delta r_{\rm po}^{\rm out}$	0.5

[a]Normalized to the outer radius of the nebula.

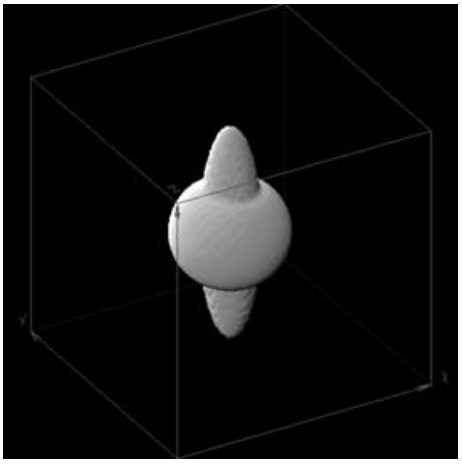

Figure 4. Three-dimensional isodensity plot of the spindle-like density distribution for model B. The density cut was chosen in order to show the shape of the inner shell of the nebula.

Table 10. Input parameters for the spindle-like models of NGC 3918.[a]

L_*(A)	6900 $L_\odot$	N/H	1.5×10^{-4}
L_*(B)	5780 $L_\odot$	O/H	5.0×10^{-4}
R_{in}	0.0 pc	Ne/H	1.2×10^{-4}
R_{out}	0.106 pc	Mg/H	1.4×10^{-4}
T_{eff}	140 000 K	Si/H	1.0×10^{-4}
log g	7.5	S/H	1.6×10^{-4}
He/H	0.107	Ar/H	2.0×10^{-4}
C/H	8.0×10^{-4}	Fe/H	3.7×10^{-4}

[a]The abundances are given by number, relative to H.

models A and B. Finally, $F_*(1300\ \text{Å}) = 2.9 \times 10^{-12}$ erg cm^{-2} s^{-1} Å^{-1} ($L_* = 6900\ L_\odot$) was chosen for model A and $F_*(1300\ \text{Å}) = 2.4 \times 10^{-12}$ erg cm^{-2} s^{-1} Å^{-1} ($L_* = 5780\ L_\odot$) was chosen for model B, as these produced the best results. Table 10 summarizes the nebular and stellar parameters used for the models described in this section.

3.1 Spindle-like density distribution models: results

Table 11 lists the predicted emission-line fluxes integrated over the nebular volume for the spindle-like models A and B for NGC 3918; for comparison, the observed values are also reported in the last column of this table. The observed spectrum is reasonably reproduced by both models. The Hβ fluxes predicted by models A and B are slightly different, but they are both within 10 per cent of the observed value. The emission-line predictions for helium seem to indicate that in both models the abundance of He^{2+} is slightly overestimated, hence leaving too little He^+. However, both results are comparable to those obtained using the biconical model and indeed to the C87 results presented in Section 2.1. The major discrepancies between the two models and the observations are the same as for the biconical model case. The C IV 1549 Å and the Mg II 2800 Å resonance doublets are overestimated by large factors by the MOCASSIN models, which do not take dust absorption into account. The Si IV 1393 and 1401 Å resonance line doublet, which should also suffer from absorption by dust, does not seem to be affected. In fact if the 30 per cent attenuation predicted by Harrington et al. (1988) were to be applied to the flux of this doublet, the fit to the observations would be made worse. However, as has already been discussed in Section 2.1.1, Si IV 1393 and 1401 Å are quite weak and the flux measured might not be accurate. As before, large discrepancies with the observations, of factors of about 10, are also observed for the [Ne V] fine-structure lines, namely [Ne V] 14.3 μm and [Ne V] 24.3 μm; this is discussed in Appendices B and C. The large discrepancies found between the spindle-like model predictions for the infrared line fluxes on the one hand, and the *ISO* SWS measurements of Bower (2001) reported in Table 11 on the other, are

Table 11. Observed and predicted emission-line fluxes for NGC 3918 (spindle-like models).

	Predicted			
Line	A	B	Observed	Ref.[a]
$H_\beta/10^{-10}$ erg cm^{-2}s^{-1}	2.19	2.58	2.34	b
H_β 4861	100	100	100	–
He I 5876	8.15	7.56	10.81	a
He II 4686	57.2	53.6	41.65	a
C II] 2326	34.6	27.8	31.24	a
C II 4267	0.23	0.21	0.50	a
[C II] 157.74 μm	0.22	0.10	0.21	c
C III] 1908	543	480	492.5	a
C III 4648	0.89	0.98	0.42	a
C III] 2297	10.2	11.3	5:	e
C IV 1550[b]	2267	2220	457.6	a
C IV 4658	0.37	0.37	0.35	a
[N I] 5199	1.03	0.46	0.63	a
[N II] 6584	41.8	33.9	84	a
N III] 1751	22.9	20.2	26.7	a
[N III] 57.3 μm	7.41	9.16	13.5	c
N IV] 1486	61.4	59.3	46.4	a
N V 1240[b]	45.6	38.7	41.4	a
[O I] 6300	3.95	2.57	5.24	a
[O I] 63.12 μm	0.40	0.26	6.72	c
[O I] 145.5 μm	0.029	0.014	0.23	c
[O II] 3727	42.7	37.9	94.5	a
[O III] 51.8 μm	79.4	112	88.6	c
[O III] 88.4 μm	14.2	22.2	27.5	c
[O III] 5007	1760	1789	1657	a
[O III] 4363	25.0	24.8	21.6	a
[O IV] 25.9 μm	352	365	89	d
O IV] 1402	34.9	31.8	48.9	a
O IV 1342	1.87	1.72	2:	e
[Ne II] 12.8 μm	1.61	0.75	12:	f
[Ne III] 15.6 μm	123	127	46.3	d
[Ne III] 3869	174	173	135.5	a
[Ne IV] 2423	89.2	87.5	132	e
[Ne V] 3426	108	99.1	80	e
[Ne V] 14.3 μm	267	256	19.6	d
[Ne V] 24.3 μm	170	146	23.1	d
[Ne VI] 7.6 μm	62.0	54.4	–	–
Mg I] 4565	0.32	0.33	0.13	a
Mg II 2800[b]	47.2	36.7	$\leqslant$1	e
[Mg IV] 4.49 μm	4.25	5.10	–	–
[Mg V] 2783	4.84	5.02	5.6	e
[Mg V] 5.6 μm	12.5	14.1	–	–
Si III] 1887	13.9	11.2	8	e
Si IV 1399[b]	11.5	10.2	9	e
[S II] 4070	1.90	1.42	2.69	a
[S III] 18.7 μm	16.6	14.3	8.7	d
[S III] 33.6 μm	5.21	4.68	–	–
[S III] 6312	1.98	1.55	2.27	a
[S IV] 10.5 μm	198	213	35.0	d

[a]References: a, Tsamis et al. (2003); b, Cahn et al. (1992); c, Liu et al. (2001); d, Bower (2001); e, C87; f, Pottasch et al. (1986).
[b]Attenuated by dust absorption.

most probably due to the *ISO* SWS aperture having been offset from the centre of the nebula. This is discussed in more detail in Section 4 and Appendix C. In general, the integrated spectra obtained from the spindle-like models are in good agreement with those obtained from MOCASSIN's biconical model, and, therefore, comments made during the discussion of the latter (Section 2.1) largely apply to the models A and B discussed in this section. The diagnostic line ratios calculated for models A and B are given in Table 12. They are in satisfactory agreement with the observed ratios, also reported in the same table, with model B providing the slightly better fit.

Table 12. Diagnostic ratios for the electron density, N_e, and electron temperature, T_e (NGC 3918 spindle-like models).

Ion[a]	Lines (Å)	Ratio Moc. A	Moc. B	C87	Obs.	Obs. ref.[b]
N_e						
Mg I	4562/4571	0.38	0.40	0.42:	0.28	1
S II	6716/6731	0.65	0.60	0.70	0.57	1
O II	3726/3729	1.96	2.02	1.61	1.98	2
O II	7325/3727[c]	0.11	0.11	–	0.0783	1
C III	1906/1909	1.25	1.34	1.36	1.31	2
Si III	1883/1892	1.15	1.31	1.30	1.37	2
Ne IV	2421/2424	1.09	1.06	0.93	1.00	2
N IV	1483/1486	1.45	1.47	1.87	1.85	2
O IV	1401/1404	1.32	1.36	1.14	1.50	2
T_e						
N II	5755/6584	0.021	0.023	0.025	0.021	1
S II	4073/6724[d]	0.200	0.245	–	0.339	1
C^{2+}	4267/1908	0.0004	0.0004	0.0005	0.0008	2
S III	6312/9532	0.032	0.032	0.029	0.032	2
O III	4363/5007	0.014	0.014	0.013	0.013	1
Ne IV	1602/2423	0.053	0.050	0.049	0.047	2
Ne V	1575/3426	0.009	0.009	0.012	0.007:	2

[a]In order of increasing ionization potential.
[b]References: 1, Tsamis et al. (2003); 2, C87.
[c](7321+7332)/(3726+3729).
[d](4068+4076)/(6717+6731).

Table 13. Fractional ionic abundances for NGC 3918 (spindle-like models of NGC 3918).[a]

Element	Ion I	II	III	IV	V	VI	VII
H	0.14 (−1)	0.986					
	0.85 (−2)	0.991					
He	0.64 (−2)	0.509	0.485				
	0.32 (−2)	0.513	0.483				
C	0.73 (−4)	0.33 (−1)	0.284	0.462	0.221		
	0.96 (−4)	0.23 (−1)	0.258	0.509	0.210		
N	0.53 (−2)	0.32 (−1)	0.279	0.501	0.129	0.053	
	0.23 (−2)	0.25 (−1)	0.256	0.544	0.125	0.047	
O	0.13 (−1)	0.28 (−1)	0.544	0.250	0.120	0.038	0.62 (−2)
	0.71 (−2)	0.24 (−1)	0.562	0.257	0.112	0.033	0.52 (−2)
Ne	0.68 (−3)	0.14 (−1)	0.553	0.195	0.192	0.045	0.99 (−3)
	0.12 (−3)	0.66 (−2)	0.560	0.207	0.186	0.039	0.92 (−3)
S	0.11 (−4)	0.21 (−1)	0.116	0.295	0.386	0.149	0.032
	0.15 (−4)	0.13 (−1)	0.094	0.276	0.445	0.144	0.028
Si	0.81 (−4)	0.133	0.128	0.247	0.211	0.211	0.070
	0.84 (−4)	0.101	0.110	0.243	0.249	0.230	0.068
Mg	0.15 (−2)	0.59 (−1)	0.351	0.123	0.179	0.225	0.060
	0.15 (−2)	0.44 (−1)	0.313	0.149	0.203	0.233	0.056

[a]For each element the upper row is for model A and the lower row is for model B.

Table 14. Mean temperatures (K) weighted by ionic species for NGC 3918 (spindle-like models of NGC 3918).[a]

Element	Ion I	II	III	IV	V	VI	VII
H	10 142	13 739					
	10 763	13 593					
He	9 795	12 430	15 061				
	10 519	12 457	14 770				
C	10 683	10 715	12 521	13 733	15 539		
	10 945	11 193	12 484	13 518	15 278		
N	9 254	10 853	12 653	13 805	15 381	16 088	
	9 805	11 239	12 606	13 594	15 085	15 924	
O	9 606	11 256	12 729	14 939	15 524	16 020	17 278
	10 188	11 518	12 689	14 656	15 288	15 792	17 839
Ne	9 093	10 202	12 603	14 771	15 422	16 004	17 881
	9 663	11 186	12 574	14 464	15 149	15 785	19 909
S	10 487	10 207	11 871	12 801	14 221	15 434	16 218
	10 872	10 796	11 840	12 712	13 875	15 133	16 117
Si	11 636	11 557	12 579	13 117	14 308	15 081	15 736
	11 628	11 652	12 443	12 968	13 935	14 655	15 381
Mg	11 403	11 189	12 197	13 730	14 759	15 250	15 812
	11 446	11 456	12 106	13 338	14 384	14 902	15 529

[a]For each element the upper row is for model A and the lower row is for model B.

Tables 13 and 14 list, respectively, the fractional ionic abundances, $f(X^i)$, and the mean electron temperatures weighted by ionic species, for the spindle-like distribution models of NGC 3918. For each element listed in the two tables, the upper entry is for model A and the lower entry is for model B. It is difficult to make a comparison with MOCASSIN's biconical model results or with those of C87, since both of the spindle-like models consist of a continuously varying gas density distribution where clear edges do not exist. The values of the ionic fractions reported in Table 13 were obtained from equation (2), and represent an average over the whole ionized volume of the local ionic fractions weighted by the local density. Figs 5 and 6 show the ionic fractions of oxygen (middle panels) and carbon (bottom panels) as a function of radius along the polar (left panels) and equatorial (right panels) directions for the spindle-like models A and B, respectively. The electron density distribution along the two directions is also shown in the top panels of Figs 5 and 6 for the polar (left panel) and equatorial (right panel) directions. It is clear from the figures that the ion distributions are very different along the two directions of each model, according to the gas density structure. Integrated ionic fractions, $f(X^i)$, such as those listed in Table 13, are very useful when discussing the large-scale ionization structure of models with density variations. However, plots of the type shown in Figs 5 and 6 can provide a better insight into the actual ionization topography of a model.

As shown in Table 14, the weighted mean temperatures calculated by MOCASSIN for model B (lower entries) are consistently lower than those calculated for model A (upper entries), apart from the third and fourth column values (for doubly and triply ionized species), which are, on the contrary, higher for model B. It is also evident that the scatter of values for the same column of ionic stage is larger for model B even for the lower ionization stages, while the scatter is very small for model A. The effects of density distributions on the final values obtained for the mean weighted temperatures have already been discussed in Section 2.2. It is clear that in this case the behaviour of the two models depends heavily on their density distributions.

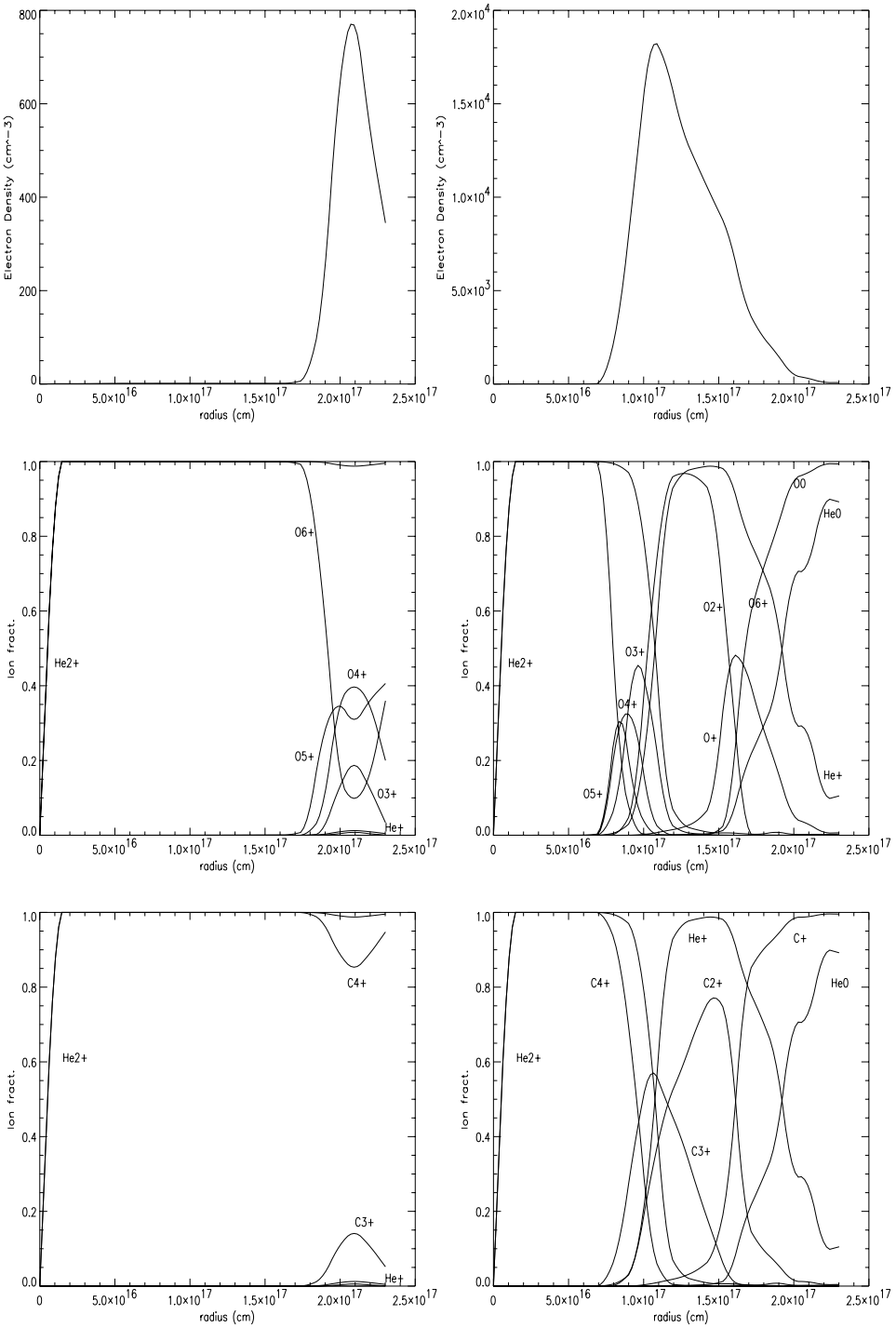

Figure 5. Ionic fractions for oxygen (middle panels) and carbon (bottom panels) along the polar (left panels) and equatorial (right panels) directions. The ionization structure of helium is also plotted in each panel. The top panels show the electron density plotted as a function of radius along the polar (top left) and equatorial (top right) directions. Spindle-like model A for NGC 3918.

4 THE INFRARED FINE-STRUCTURE LINE FLUX DISCREPANCIES

The main reason for the discrepancy observed between the models' predictions of the infrared line fluxes and the Bower (2001) measurements from the *ISO* SWS data for NGC 3918 is that the nebular coordinates used for the *ISO* observations were incorrect by approximately 14 arcsec (see Appendix C). A *masking* Interactive Data Language (IDL) routine (Morisset et al. 2002), which makes use of the measured wavelength-dependent SWS beam profiles, was applied to the projected maps obtained from the final converged model grids, in the six infrared fine-structure lines. This routine returns a *mask* which takes into account the wavelength-dependent aperture size and beam profile, and which can then be applied to a map of the object in the required emission line to predict the emergent flux that would be measured. The position of the aperture centre was

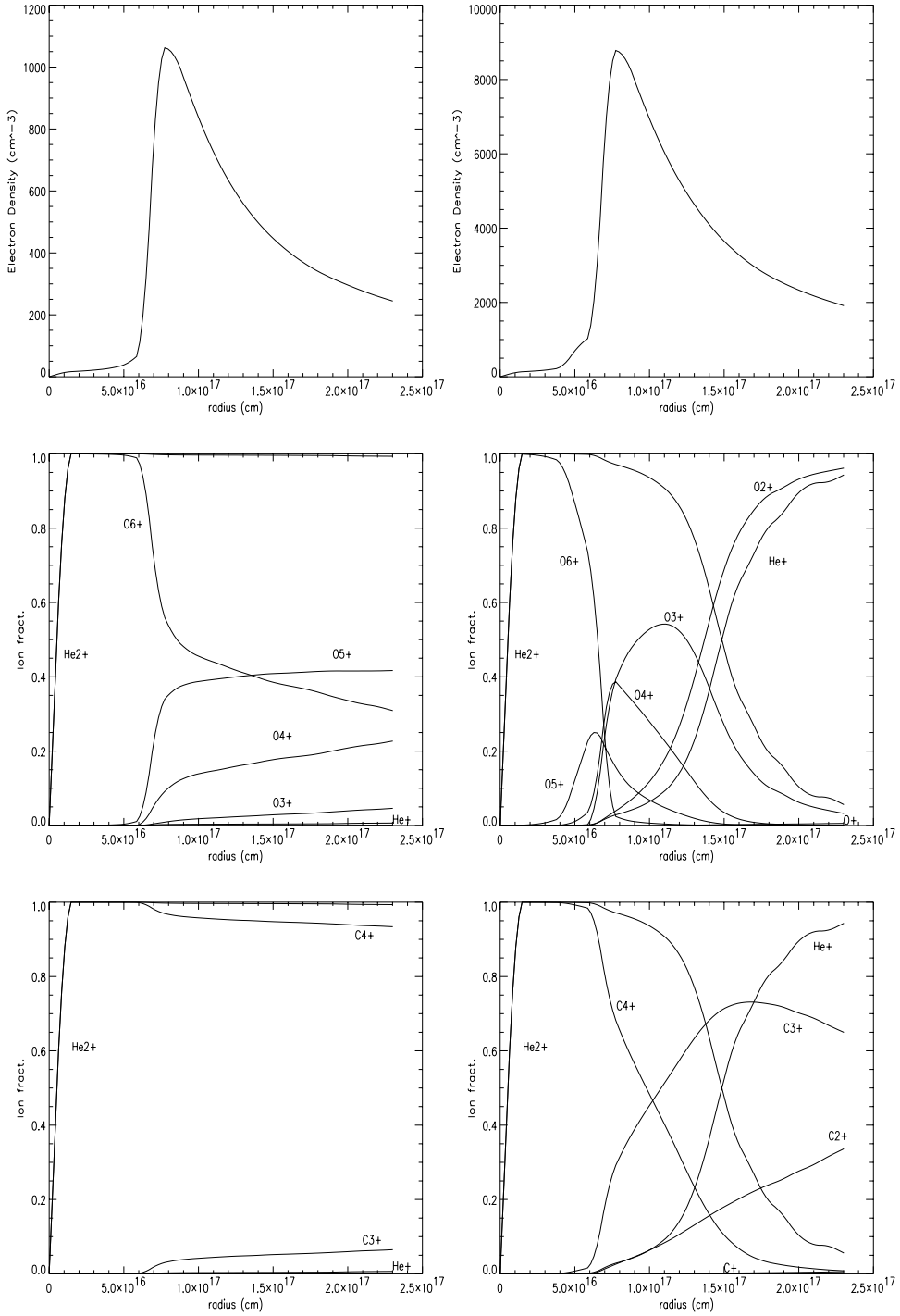

Figure 6. Ionic fractions for oxygen (middle panels) and carbon (bottom panels) along the polar (left panels) and equatorial (right panels) directions. The ionization structure of helium is also plotted in each panel. The top panels show the electron density plotted as a function of radius along the polar (top left) and equatorial (top right) directions. Spindle-like model B for NGC 3918.

offset from the centre of the nebula by the amounts specified above, and the aperture was rotated by an angle of 80° east of north[1] to correspond to the spacecraft roll angle. Resultant predicted fluxes were obtained by convolution of the offset, rotated mask with the correctly oriented map of NGC 3918 in the required emission line.

Table 15 provides a summary of the line fluxes predicted for the six infrared fine-structure lines, first for the whole nebula, i.e. without the aperture corrections (column 2) and then after the corrections for the aperture profile, offset and orientation (column 3). Fig. 7 illustrates the effects of the aperture corrections on the final transmitted flux for three of the six infrared fine-structure lines for

[1] From the *ISO* archive, CINSTROLL = 350°, where CINST–ROLL is the instrument's roll angle, defined as the angle anticlockwise between north and the spacecraft z-axis. Since the long axis of the SWS apertures is in the y-direction and the short axis is in the z-direction, then PA = CINSTROLL + 90°.

Table 15. Predicted infrared line fluxes from NGC 3918 corrected for the *ISO* SWS beam profile and pointing position.

Line	Model predictions		Observed[a]
	Uncorr.	Corr.	
Biconical model[b]			
[O IV] 25.9 μm	352	96.1	89.0
[Ne III] 15.6 μm	131	33.6	46.3
[Ne V] 14.3 μm	286	69.7	19.6
[Ne V] 24.3 μm	220	60.1	23.1
[S III] 18.7 μm	48	14.3	8.7
[S IV] 10.5 μm	220	86.1	35.0
Spindle-like A[c]			
[O IV] 25.9 μm	352	100	89.0
[Ne III] 15.6 μm	122	21.8	46.3
[Ne V] 14.3 μm	268	68.9	19.6
[Ne V] 24.3 μm	170	49.4	23.1
[S III] 18.7 μm	27	5.9	8.7
[S IV] 10.5 μm	255	91.5	35.0
Spindle-like B[d]			
[O IV] 25.9 μm	364	104	89.0
[Ne III] 15.6 μm	126	40.8	46.3
[Ne V] 14.3 μm	256	58.0	19.6
[Ne V] 24.3 μm	146	40.9	23.1
[S III] 18.7 μm	27	10.0	8.7
[S IV] 10.5 μm	302	114	35.0

[a]The fluxes are given on a scale relative to H$\beta = 100$, where $I(\mathrm{H}\,\beta) = 2.34 \times 10^{-10}$ erg cm^{-2} s^{-1}.
[b]The fluxes are given on a scale relative to H$\beta = 100$, where $I(\mathrm{H}\,\beta) = 2.33 \times 10^{-10}$ erg cm^{-2} s^{-1}.
[c]The fluxes are given on a scale relative to H$\beta = 100$, where $I(\mathrm{H}\,\beta) = 2.20 \times 10^{-10}$ erg cm^{-2} s^{-1}.
[d]The fluxes are given on a scale relative to H$\beta = 100$, where $I(\mathrm{H}\,\beta) = 2.56 \times 10^{-10}$ erg cm^{-2} s^{-1}.

the spindle-like model B of NGC 3918, namely [O IV] 25.9 μm, [Ne III] 15.6 μm and [S III] 18.7 μm. The upper panel of each pair shows a map of NGC 3918 in a particular infrared fine-structure emission line, oriented such that north is up and east is to the left; a contour map of the appropriate wavelength-dependent aperture transmission profile is superimposed on each map. The lower panel of each pair shows the map from the corresponding upper panel *after* convolution with the appropriate *ISO* SWS aperture profile.

It is clear from the images, and from the corrected line fluxes reported in Table 15, that the SWS aperture offset is indeed the main reason for the SWS infrared line flux discrepancy. However, even after these corrections the fluxes for the predicted [Ne V] fine structure lines are still a factor of 2–3 too strong compared to the observed values; this may be due to the collision strengths by Lennon & Burke (1991) used in the MOCASSIN code, which are much larger than those used in the Harrington code by C87. This has already been discussed in Section 2.1. A discrepancy also remains between the SWS flux in the [S IV] 10.5 μm line measured by Bower (2001) and the corrected fluxes predicted by MOCASSIN, which are a factor of 2–3 stronger. C87 also predicted a flux for this line which was a factor of 3.6 stronger than the *IRAS* LRS measurements of Pottasch et al. (1986). The origin of this discrepancy still remains unclear.

It is worth noting that, although the aperture offset of 14 arcsec also applied to the LWS observations made with *ISO* (Liu et al. 2001), this would not affect the integrated flux measurements, as a result of the much larger aperture size of the LWS (≈70–80 arcsec full width at half-maximum, FWHM).

5 VISUALIZATION OF THE MODEL RESULTS

A large amount of observational data has been obtained for NGC 3918 over the years. Some of the most recent data published

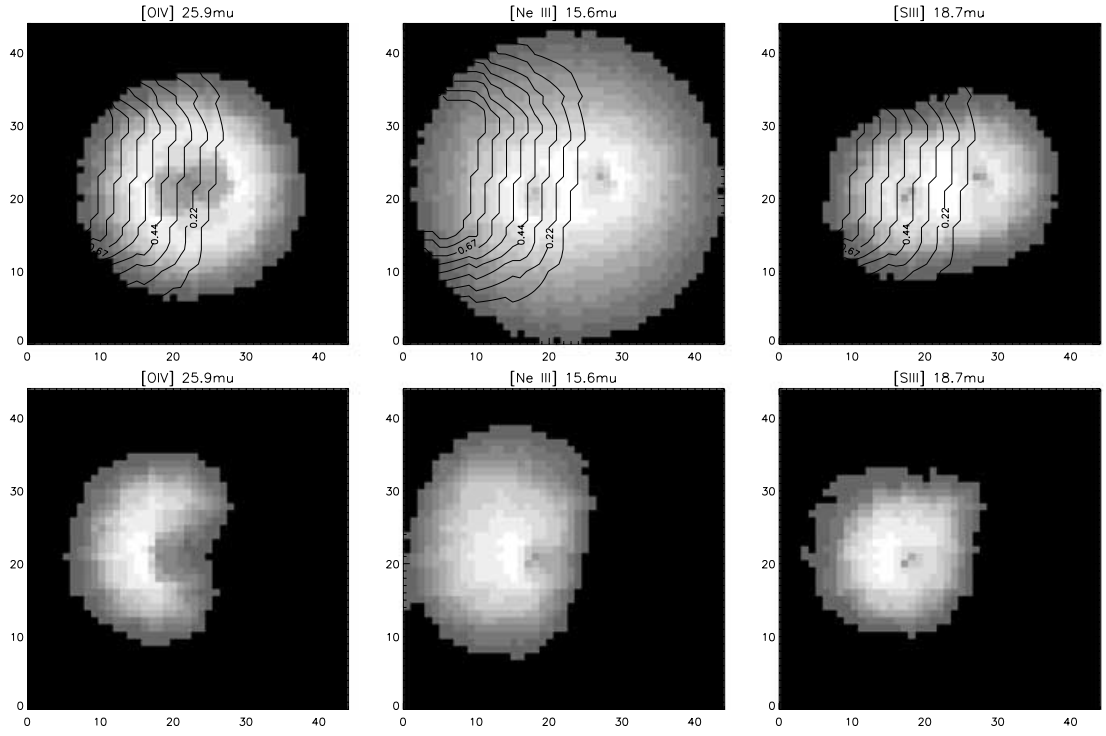

Figure 7. Predicted projected images of NGC 3918 in three infrared fine-structure lines observed by the *ISO* SWS, for the spindle-like model B. The upper panels show contour plots of the *ISO* SWS apertures' transmission efficiency superimposed on to the map in the given emission line. The lower panels contain the projected maps of the nebula in each line after convolution with the aperture response maps. All the images are oriented such that north is up and east to the left.

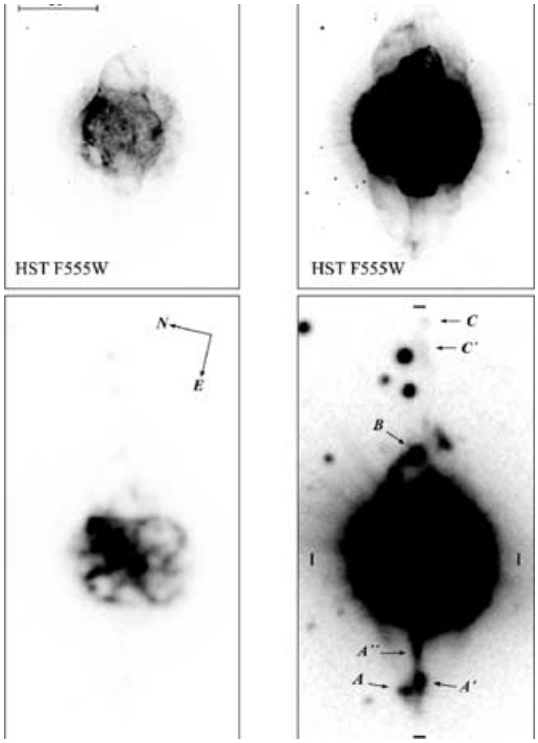

Figure 8. *HST* and NTT images of NGC 3918 (Corradi et al. 1999). The images are rotated so as to have the main jet-like feature oriented along the vertical direction, and are displayed to show the highest intensity levels using a linear scale (left) and the faintest structures using a logarithmic scale (right).

include the optical images and the high-resolution, long-slit spectra presented by C99. In the same paper they also presented an image of NGC 3918, retrieved from the *HST* archives, and obtained in 1995 with the Wide Field Planetary Camera 2 (WFPC2) in the F555W filter and shown here in Fig. 8. C99 claimed that the emission in this image (central wavelength 5252 Å, FWHM 1223 Å) is dominated by [O III] 4959+5007 Å; however, many other nebular lines, including Hβ, He I 5876 Å, He II 4686 Å, [Ar IV] 4711,4740 Å and [N II] 5755 Å, fall within the transmission range of this filter, and, although weaker than the [O III] lines, can be important at particular positions in the nebula.

5.1 Projected images

In order to compare the final model results for the biconical distribution and for the spindle-like distribution, IDL visualization routines, described by Morisset, Gruenwald & Viegas (2000) and Monteiro et al. (2000), were employed. Fig. 9 shows predicted maps of NGC 3918 in the Hβ emission line, obtained from the three models developed in this work; namely, the biconical model (left-hand panels) and the spindle-like models A (central panels) and B (right-hand panels). The bottom panels of Fig. 9 display the maps on a logarithmic scale.

The inclination and spatio-kinematical parameters of NGC 3918 were derived by C99 using the spatio-kinematical model of Solf & Ulrich (1985). They obtained the best fit to the observed shape and kinematics of the inner shell by assuming an inclination angle θ of 75°, where θ is defined as the angle between the polar axis and the line of sight. The data cubes calculated in this work for the spindle-like models A and B were, therefore, rotated through the same angle to produce projected maps in various emission lines, including those shown in Fig. 9. C87 derived some kinematical information from a Coudé spectrum of the [O II] $\lambda\lambda$3726,3729 doublet. From this they derived an inclination angle, θ, for the biconical density distribution model, of 15°. Therefore the projected images for the biconical model (including the Hβ maps shown in Fig. 9) were obtained by rotating the grid by the same angle. The images of NGC 3918 published by C99 also show some low-intensity small-scale features associated with this object. In our work, however, no attempt was made to reproduce these features. They are discussed in more detail

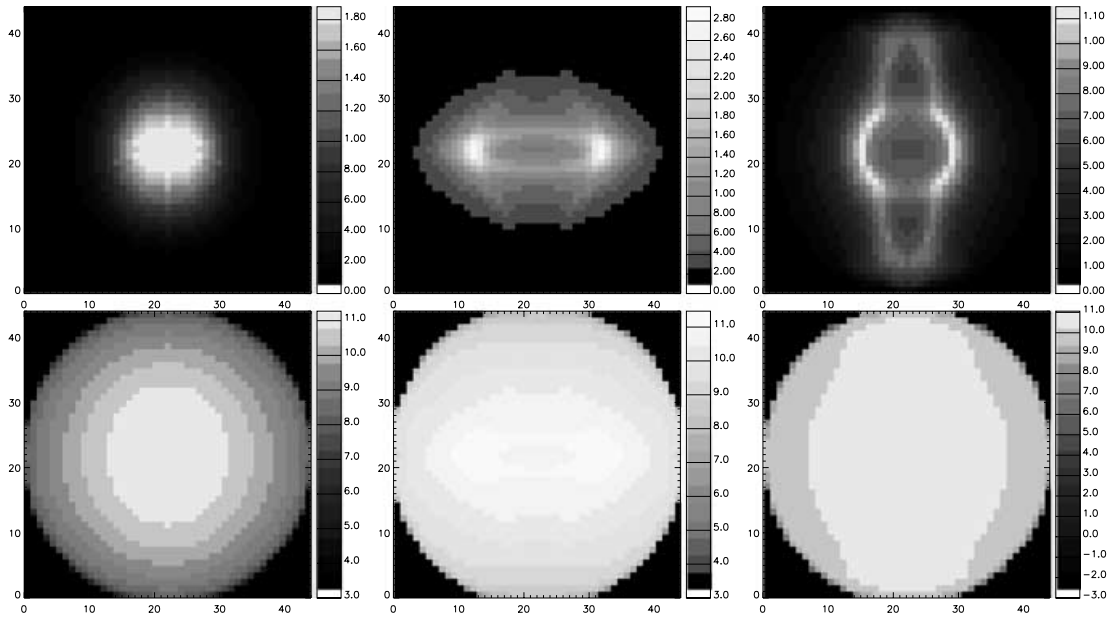

Figure 9. Projected maps of NGC 3918 in Hβ for the biconical model (left panels), the spindle-like model A (central panels) and the spindle-like model B (right panels). The top panels are displayed with linear intensity scales and the bottom panels are displayed on logarithmic scales. The spatial units are pixels and the intensity range is in arbitrary units. Note that a different 'grey-scale' has been used for the spindle-like model A maps, in order to highlight some of the features.

by C99, including several low-ionization structures located roughly along the major axis of the nebula and clearly visible in the logarithmic [N II] image (fig. 1 of C99, bottom right), where they are labelled with the letters A, A′, A″, B, C and C″. The shape of the inner shell, described in Section 1, is more clearly visible in the *HST* images (e.g. Fig. 8), while the lower angular resolution NTT image in [N II] (fig. 1 of C99, bottom left) shows an almost filamentary distribution.

From the projected maps obtained in several emission lines for the biconical density distribution model (the Hβ maps are shown in the left-hand panels of Fig. 9), it became obvious that the model proposed by C87, although successful in reproducing the emission spectrum of NGC 3918, cannot be used actually to describe the geometric structure of this object. C87, however, were right to assume that this object must be optically thick in some directions and optically thin in others, in order to obtain such a complex spectrum, exhibiting strong emission lines from a wide range of ionization stages, e.g. [Ne V] and He II to [O I] and [N I]. A number of combinations of thick and thin phases could possibly have been used to construct models to fit the emission lines and, without additional spatial information, it would have been virtually impossible to distinguish between them.

Projected maps were also obtained in several emission lines for the density distribution given by the Mellema (1996) model (spindle-like model A), discussed in Section 3. Once again, for the sake of space, only the Hβ maps are shown in Fig. 9 (central panels). As discussed in the previous section, the original distribution had to be enhanced in the equatorial region in order to reproduce the observed spectrum correctly. Although the shape of the inner shell of NGC 3918 is reproduced better than by the biconical model, the polar protrusions were still missing and the enhancement seemed to be too localized in a small equatorial torus.

The best matches to the observed images of NGC 3918 were obtained for the spindle-like model B, where the density distribution of the inner shell was reproduced using the analytical expression given in Appendix A. Fig. 9 (right-hand panels) shows the Hβ maps obtained for this model on a linear scale (top) and a logarithmic scale (bottom). The detailed shape and density distribution given by the analytical description depends on 10 parameters, and it is possible that a number of combinations of these could be used to reproduce the observations. However, the combination used in this model (see Table 9) produces images (Fig. 9) and spectroscopic results (see below) which are consistent with the observations. It might be possible to obtain even better fits by further adjusting the density distribution parameters and, possibly, also the central star parameters, considering that those obtained by C87 were based on a completely different geometrical model. The central star parameters, however, were based on global nebular properties which should not change as much.

5.2 Position–velocity diagrams and line profiles

As mentioned above, C99 used the spatio-kinematical empirical model of Solf & Ulrich (1985) to describe the nebular expansion velocity, $V_{\rm exp}$, in order to fit their observations of position velocity plots of Hα and the shape of the inner shell of NGC 3918. In this model $V_{\rm exp}$ increases from the equatorial plane towards the polar axis according to the equation (Solf & Ulrich 1985)

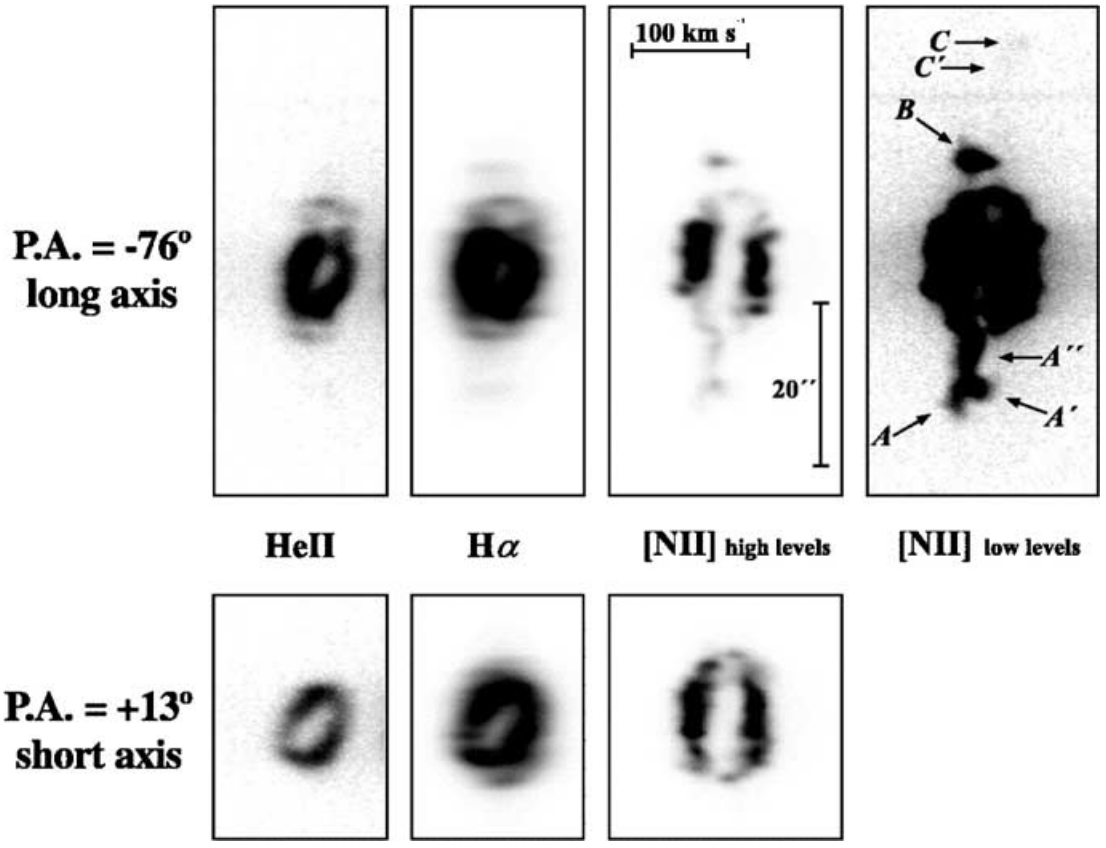

Figure 10. NTT long-slit spectra of NGC 3918. Images are in a logarithmic intensity scale with different cuts for the He II 6560 Å, Hα and [N II] 6584 Å (C99).

$$V_{\rm exp}(\phi) = V_{\rm e} + (V_{\rm p} - V_{\rm e}) \sin^{\gamma} |\phi|, \quad (5)$$

where ϕ is the latitude angle, defined such that $\phi = 0^{\circ}$ in the equatorial plane and $\phi = 90^{\circ}$ in the polar direction; $V_{\rm p}$ and $V_{\rm e}$ are the equatorial and polar velocity components, respectively ($V_{\rm p} = 50$ km s^{-1} and $V_{\rm e} = 23$ km s^{-1} in their work); and γ is a shape parameter ($\gamma = 12$ in their work). Here the velocity field described above was used for the spindle-like density distribution model A in order to produce position–velocity diagrams along slits positioned at PA $= -76^{\circ}$ and PA $= +13^{\circ}$, in order to compare with C99's observations, shown in Fig. 10. Position–velocity diagrams were obtained for each of the lines with long-slit spectra presented by C99, and include He II λ4686, Hα and [N II] λ6584. These are shown in Fig. 11 (middle two rows).

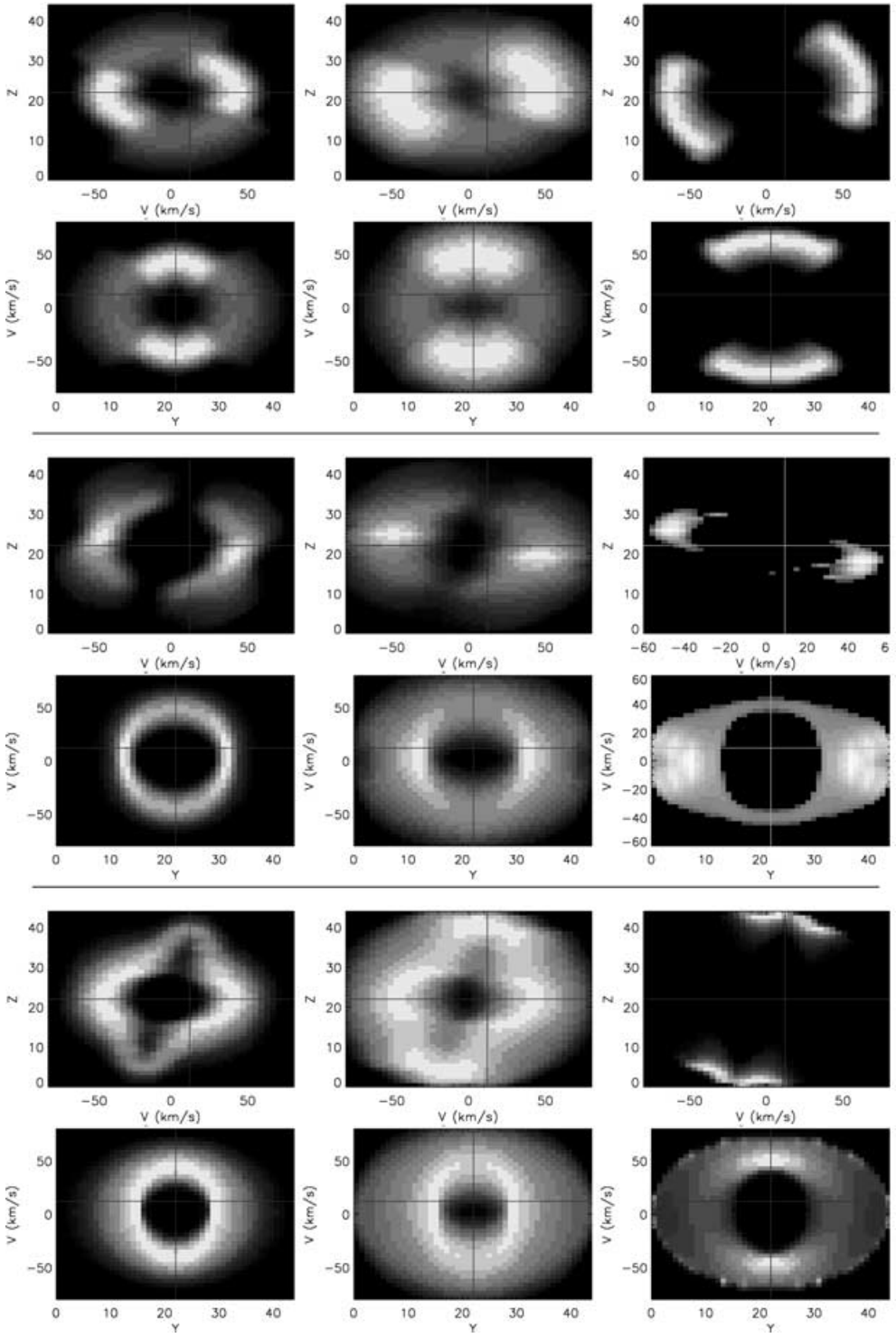

Figure 11. Position–velocity diagrams in He II 4686Å (left panels), Hα (central panels) and [N II] 6584Å (right panels) for the biconical model (top two rows), spindle-like model A (middle two rows) and spindle-like model B (bottom two rows) of NGC 3918. The top panels in each pair of rows show the echellograms obtained with slits oriented at PA $= -76^{\circ}$ while the bottom diagrams show echellograms obtained in the same lines, but with slits positioned at PA $= +13^{\circ}$.

Position–velocity maps were also produced for the biconical density distribution model and for spindle-like model B (Fig. 11, top two rows and bottom two rows, respectively) using the same slit positions as above. A simple radial velocity field was adopted, namely

$$V(r) = V_0 + V_1 r, \quad (6)$$

where r is the radial distance, and V_0 and V_1 are constants ($V_0 =$ 23 km s^{-1} and $V_1 = 50$ km s^{-1} in this work). Originally, the Solf & Ulrich (1985) description of the velocity field was also used for spindle-like model B; however, it was found that better matching results were obtained by using the simple radial velocity field described above, which was applied to obtain the echellograms shown in Fig. 11. The Solf & Ulrich (1985) kinematical model does not seem to work well with the analytical density distribution used for model B. The disagreement is particularly evident in the major axis position–velocity diagrams, where the polar enhancement of the velocity field creates two bright spots which have not been observed. The same does not happen when the Solf & Ulrich (1985) velocity field is applied to the spindle-like model A, since the two polar protrusions (which are created in model B by embedding an elliptical shell within a spheroid) are *not closed* at the poles (see Fig. 1). However, from the *HST* image shown in the left-hand panel of Fig. 8, it seems that the polar protrusions are indeed *closed*, although not very dense, and therefore the density distribution used in model B seems more appropriate.

After inspection of all the position–velocity diagrams obtained for the three models (Fig. 11) and comparison with C99's fig. 4, it is clear that the observations are most closely reproduced by the spindle-like model B (bottom two rows in Fig. 11). All the synthetic position–velocity diagrams are plotted on a logarithmic intensity scale. It is worth noting at this point that all minor axis position–velocity diagrams (bottom panels in each pair of rows) are plotted such that the ordinate is the velocity (in km s^{-1}) and the abscissa is the spatial variable; this has to be taken into account when comparing the synthetic spectra to the observations in Fig. 10, where the abscissa and the ordinate are reversed. The [N II] position velocity diagrams show the largest discrepancies and will be discussed below. Before that, however, we will focus on the Hα and He II position–velocity diagrams. The projected maps (Fig. 9) had already anticipated, and the synthetic echellograms in Fig. 11 (top two rows) confirmed, that the biconical distribution is not a realistic representation of NGC 3918. However, as already mentioned, the imaging information available for NGC 3918 was very limited at the time when this model was devised by C87. Model A (middle two rows of the position–velocity diagrams in Fig. 11) fails to reproduce the polar protrusions in the observed long-slit spectra (Fig. 10), as was also clear from the projected maps obtained from this model (Fig. 9, central panels). Moreover, the thick waist in model A, which had to be artificially created in order to obtain the observed linestrengths for the lower ionization species, is not observed in NGC 3918.

None of the models presented in this work succeeded in reproducing the [N II] λ6584 echellograms shown in Fig. 10. There are two main reasons for the observed discrepancies. First, N^+ is abundant in the fast, low-ionization emitting regions (FLIERs) of NGC 3918 (C99), which are not accounted for in the models presented here. Secondly, N^+ also seems to exist in the inner regions of the shell; the NTT image in fig. 1 of C99 shows [N II] emission to be present in almost a *filamentary* form. All the models presented in this work have *smooth* density distributions and do not include any filaments or knots. In spindle-like model A, N^+ is mainly concentrated in the toroidal region behind the thick equatorial waist, which is screened from direct starlight, whereas in model B, N^+ is mostly concentrated in small polar regions beyond the elliptical shell which creates the protrusion, and they are also screened from direct starlight by this shell and are further away from the star. In fact, it is quite hard to have N^+ *survive* in the very hard stellar radiation field ($T_{\rm eff} =$ 140 000 K) in the inner shell, unless some sort of density enhancement is postulated. This shows that, although spindle-like model B appears to be quite successful in reproducing the main spectroscopic and kinematic characteristics of NGC 3918, there is still scope for improvement.

A three-dimensional reconstruction technique for studying the morphology, physical condition, ionization and spatial structure of planetary nebulae has been introduced by Sabbadin et al. (2000a); Sabbadin et al. (2000b) and Ragazzoni et al. (2001). In this approach, the relative density distribution of an emitting region along the cross-section of nebula covered by the slit can be obtained from the radial velocity, the FWHM and the intensity profile. Sabaddin and other members of the Padova group have recently obtained observations for several other planetary nebulae, including NGC 3918, consisting of long-slit echellograms at various position angles on the nebulae, and are planning to carry out detailed studies of them by applying their three-dimensional reconstruction technique to them. This means that in the near future a *data cube* containing a three-dimensional density distribution obtained using the method above could be available for NGC 3918. It would be very interesting then to map such a data cube on to a MOCASSIN grid and construct a new photoionization model for this object, since as discussed earlier, although spindle-like model B produces satisfactory results, there are still some discrepancies remaining with the observational data.

6 CONCLUSIONS

In this paper three photoionization models were constructed for the planetary nebula NGC 3918, a biconical model and two spindle-like models. The first spindle-like model (A) used the density distribution of the Mellema (1996) model already applied to this object by C99. The second spindle-like model (B) instead used an analytical expression for the density distribution, which aimed to mimic, by means of an ellipsoid embedded in a sphere, the shape of the inner shell of NGC 3918. The aim was to find a model that could reproduce not only the main spectroscopic features observed for this object, but also the spatio-kinematical properties of the nebula which recent observations (C99) have uncovered.

The integrated emission-line spectra obtained from the three different models were all in fair agreement with the observations. Discrepancies exist between the observed line fluxes of the C IV $\lambda\lambda$1548,1550 and Mg II $\lambda\lambda$2796,2803 resonance doublets, which can largely be explained by dust absorption in the nebula (Harrington et al. 1988). Large discrepancies were also found between the models' predictions for the fluxes of the infrared fine-structure lines and the measurements of the *ISO* SWS spectra. The main cause for this discrepancy is a pointing error which affected *ISO* observations of NGC 3918, causing an offset of approximately 14 arcsec from the centre of the nebula. The corrected predicted line fluxes, obtained by convolving the *ISO* SWS aperture profiles with projected nebular maps in the relevant emission lines, confirmed that most of the discrepancy between the observed and model fluxes could be attributed to the pointing error, although there is still a factor of 3 discrepancy for the [S IV] 10.5 μm line.

A diffuse radiation field consistency test was also carried out in this work, which showed that the interaction of the diffuse radiation fields from two adjacent regions of different densities is not

negligible, even in the relatively uncomplicated case of the biconical density distribution used by C87. We found that the low-ionization species in the optically thick cones were particularly affected by the diffuse radiation field coming from the optically thin sector.

Although the volume-integrated emission-line spectra obtained by the three models of NGC 3918 were in agreement with each other, the projected maps and the synthetic long-slit spectra obtained in several emission lines were, however, very different from one model to the other. Spindle-like model B produced the best fits to the observations, although some discrepancies still exist, particularly in the [N II] maps and long-slit spectra, as discussed in Section 5.2.

Confirming the conclusions of Monteiro et al. (2000), from their three-dimensional modelling of NGC 3132, this work has indicated that a detailed model of a nebula cannot be verified just by comparison of the observed integrated spectrum with model predictions. In fact, in the case of NGC 3918, approximately the same spectrum can be obtained with a number of different geometries and density distributions. For this reason, three-dimensional models are necessary in order to allow a spatio-kinematical analysis to be carried out by comparing predicted images and position–velocity diagrams in several lines to available observational data. MOCASSIN provides all the tools needed for such simulations and for the visualization of the final results.

ACKNOWLEDGMENTS

We are most grateful to Dr G. Mellema for providing the density distribution file used by C99 and in our spindle-like model A of NGC 3918. We thank the anonymous referee for useful comments. BE acknowledges support from PPARC Grant PPA/G/S/1997/00728 and the award of a University of London Jubber Studentship.

REFERENCES

Aggarwal K. M., 1983, J. Phys. B, 16, 2405
Berrington K. A., 2001, in Ferland G., Savin D. W., eds, ASP Conf. Ser. Vol. 247, Spectroscopic Challenge of Photoionized Plasmas. Astron. Soc. Pac., San Francisco, p. 137
Berrington K. A., Burke P. G., Butler K., Seaton M. J., Storey P., Taylor K. T., Yan Y., 1987, J. Phys. B, 20, 6379
Bower K., 2001, Final year astronomy project, Univ. College London
Cahn J. H., Kaler J. B., Stanghellini L., 1992, A&AS, 94, 399
Clegg R. E. S., Harrington J. P., Barlow M. J., Walsh J. R., 1987, ApJ, 314, 551 (C87)
Corradi R. L. M., Perinotto M., Villaver E., Mampaso A., Gonçalves D. R., 1999, ApJ, 523, 721 (C99)
de Graaw T. et al., 1996, A&A, 315, L49
Ercolano B., 2002, PhD thesis, Univ. London
Ercolano B., Barlow M. J., Storey P. J., Liu X.-W., 2003, MNRAS, 340, 1136 (Paper I, this issue)
Griffin D. C., Badnell N. R., 2000, J. Phys. B, 33, 4389
Harrington J. P., Feibelman W. A., 1983, ApJ, 265, 258
Harrington J. P., Seaton M. J., Adams S., Lutz J. H., 1982, MNRAS, 199, 517
Harrington J. P., Monk D. J., Clegg R. E. S., 1988, MNRAS, 231, 577
Hummer D. G., Berrington K. A., Eissner W., Pradhan A. K., Saraph H. E., Tully J. A., 1993, A&A, 279, 298
Leech K. et al., 2002, The ISO Handbook, Vol. V: SWS – The Short Wavelength Spectrometer. ESA Publications Division, Noordwijk
Lennon D. J., Burke V. M., 1991, MNRAS, 251, 628
Liu X.-W. et al., 2001, MNRAS, 323, 343
Mellema G., 1996, PhD Thesis, Univ. Leiden
Mendoza C., 1983, in Flower D. R., ed., Proc. IAU Symp. 103, Planetary Nebulae. Reidel, Dordrecht, p. 143
Mihalas D., Auer L. H., 1975, NCAR-TN/STR-104
Milne D. K., 1976, AJ, 81, 753
Monteiro H., Morisset C., Gruenwald R., Viegas S. M., 2000, ApJ, 537, 853
Morisset C., Gruenwald R., Viegas S. M., 2000, ApJ, p. 533, 931
Morisset C., Schaerer D., Martín-Hernández N. L., Peeters E., Damour F., Baluteau J.-P., Cox P., Roelfsema P., 2002, A&A, 386, 558
Péquignot D. et al., 2001, in Ferland G., Savin D. W., eds, ASP Conf. Ser. Vol. 247, Spectroscopic Challenges of Photoionized Plasmas. Astron. Soc. Pac., San Francisco, p. 533
Pottasch S. R., Preite-Martinez A., Olnon F. N., Jing-Er M., Kingma S., 1986, A&A, 161, 363
Ragazzoni R., Cappellaro E., Benetti S., Turatto M., Sabbadin F., 2001, A&A, 369, 1088
Sabbadin F., Cappellaro E., Benetti S., Turatto M., Zanin C., 2000a, A&A, 355, 688
Sabbadin F., Benetti S., Cappellaro E., Turatto M., 2000b, A&A, 361, 1112
Saraph H. E., Seaton M. J., Shemming J., 1970, Phil. Trans. R. Soc. London, A 264, 77
Solf J., Ulrich H., 1985, A&A, 148, 274
Tsamis Y. G., Liu X.-W., Barlow M. J., Danziger I. J., Storey P. J., 2003, MNRAS, submitted
van Hoof P. A. M., Beintema D. A., Verner D. A., Ferland G. J., 2000, A&A, 354, 41
Verner D. A., Ferland G. J., Korista K. T., Yakovlev D. G., 1996, ApJ, 465, 487

APPENDIX A: ANALYTICAL DESCRIPTION OF SPINDLE-LIKE MODEL B

We define the following *cut* functions:

$$C_{01}(x, x_0, \Delta x) = 0.5 + \frac{1}{\pi}\tan^{-1}\left(\frac{x - x_0}{\Delta x}\right),$$
$$C_{10}(x, x_0, \Delta x) = 0.5 - \frac{1}{\pi}\tan^{-1}\left(\frac{x - x_0}{\Delta x}\right). \quad \text{(A1)}$$

The functions above can be used to describe a smooth transition from 0 to 1 and from 1 to 0, respectively, about the value x_0, with a typical size for the transition of Δx.

The equatorial spherical shell can then be described as follows:

$$\text{equat}(r, \theta) = C_{01}(\theta, \theta_1, \Delta\theta) C_{01}\left(r, r_{\rm eq}, \Delta r_{\rm eq}^{\rm in}\right) C_{10}\left(r, r_{\rm eq}, \Delta r_{\rm eq}^{\rm out}\right), \quad \text{(A2)}$$

where r is the radial distance and θ the polar angle ($\theta = 90^\circ$ at the equator and $\theta = 0^\circ$ at the two poles). Values for θ_1, $\Delta\theta$, $r_{\rm eq}$, $\Delta r_{\rm eq}^{\rm in}$ and $\Delta r_{\rm eq}^{\rm out}$ are given in Table 9.

We then define $r_{\rm e}$, the radius of the ellipsoid, as $r_{\rm e} = \sqrt{x^2 + y^2 + (ez)^2}$, where e is the eccentricity (given in Table 9). Then the polar protrusions can be created using the following expression:

$$\text{pole}(r, \theta) = C_{10}(\theta, \theta_1, \Delta\theta) C_{01}\left(r_{\rm e}, r_{\rm po}, \Delta r_{\rm po}^{\rm in}\right) C_{10}\left(r_{\rm e}, r_{\rm po}, \Delta r_{\rm po}^{\rm out}\right), \quad \text{(A3)}$$

where $r_{\rm po}$, $\Delta r_{\rm po}^{in}$ and $\Delta r_{\rm po}^{\rm out}$ are also given in Table 9. Finally, the density distribution at any point in the grid can be obtained by combining equations (7) and (8), as follows:

$$N_{\rm H}(r, \theta) = n_1[\text{equat}(r, \theta) + \text{pole}(r, \theta)]. \quad \text{(A4)}$$

APPENDIX B: THE [NEV] FINE-STRUCTURE LINES

The largest discrepancies between this work and that of C87 were obtained for the predictions of the infrared fine-structure line fluxes of Ne^{4+}, namely [Ne V] 14.3 μm and [Ne V] 24.3 μm,

which disagree by factors of almost 10 and 5, respectively, with C87's predictions and indeed with the observations. The discrepancy between the models is due to differences in the collision strengths used for these lines. The collision strengths for these transitions used by MOCASSIN are the calculations by Lennon & Burke (1991), based on the *R*-matrix method described by Berrington et al. (1987). These collision strengths are much larger than the rates given by Mendoza (1983) based on the results of Saraph, Seaton & Shemming (1970), which were used by C87 in their model. In 1987, however, the collision strengths of Aggarwal (1983) were already available for [Ne V], and these were also much higher than those given by Mendoza (1983), since they took into account the large resonances existing at energies just above the threshold for excitation of the fine-structure lines. C87 decided against using those results as they were not in agreement with the observed ratios of [Ne V] 3426 Å/14.3 μm. However, van Hoof et al. (2000) later argued that the collision strengths calculated by Lennon & Burke (1991), which were similar to the Aggarwal (1983) values, are reliable, and that the discrepancies found by C87 can be explained by the inaccuracy of the [Ne V] 3426 Å flux that they adopted. Moreover, Berrington (2001), in his contribution to the 2000 November Lexington workshop, discussed near-threshold resonances in the calculation for collision strengths for fine-structure transitions, taking [Ne V] as a case study. He compared the effective collision strengths obtained using different methods, showing that they all largely agree with the Lennon & Burke (1991) results. During the same Lexington meeting, a new *R*-matrix calculation of [Ne V] was independently published by Griffin & Badnell (2000), who also obtained similar results. In the current work the decision to use the collision strengths of Lennon & Burke (1991), although producing results which are in disagreement with C87's observations, was finally taken, since the benchmarking carried out for the Lexington optically thick planetary nebula, which has a central star with effective temperature, $T_{\rm eff} = 150\,000$ K (similar to the central star of NGC 3918), clearly showed that most photoionization codes (all but Sutherland's MAPPINGS) use the new collision strengths (Ercolano et al. 2003).

The likely cause of the large discrepancy between the predicted and observed [Ne V] fine-structure line fluxes is addressed in Section 4 and in Appendix C below.

APPENDIX C: THE ISO POINTING ERROR

Most of the infrared line flux measurements reported in Table 2 are taken from Bower (2001) (reference 'd' in Table 2), measured from spectra taken with the *ISO* Short-Wavelength Spectrometer (SWS) between 1996 and 1998. The fluxes measured by Bower (2001) for the infrared lines of NGC 3918 are systematically smaller, by approximately a factor of 2, than those measured by Pottasch et al. (1986), who used *IRAS* Low-Resolution Spectrometer (LRS) observations and are smaller by factors of 3–6 for most lines, apart from the [Ne V] fine-structure lines, which are between 10 and 15 times smaller, compared to both MOCASSIN and C87 predictions. The reason for the [Ne V] fine-structure line discrepancy between the MOCASSIN and C87 predictions has already been discussed above. This *ISO* SWS discrepancy is also evident in the spindle-like models of NGC 3918 (see Section 3.1) and is believed to be due to the combined effects of incorrect object coordinates used for the *ISO* observations and the small size of the *ISO* SWS aperture. The *ISO* LWS fluxes for the [N III] 57.3 μm and [O III] 51.8 μm and 88.4 μm lines are in good agreement with the model predictions. Although the same pointing error of 14 arcsec occurred, the much larger LWS aperture of 70–80 arcsec minimized the effects on the observed fluxes. Corrections to the predicted *ISO* SWS line fluxes are calculated and discussed in detail in Section 4.

The position given by the Strasbourg–CDS Simbad data base for NGC 3918, in the J2000 FK5 reference frame, is $\alpha(2000) = 11^{\rm h}50^{\rm m}17\overset{\rm s}{.}2$ and $\delta(2000) = -57^\circ 10' 53''$, while the position used for the *ISO* SWS and *LWS* observations of NGC 3918 was that measured by Milne (1976), namely $\alpha(1950) = 11^{\rm h}47^{\rm m}50\overset{\rm s}{.}1$ and $\delta(1950) = -56^\circ 54' 10''$, equivalent to $\alpha(2000) = 11^{\rm h}50^{\rm m}18\overset{\rm s}{.}9$ and $\delta(2000) = -57^\circ 10' 51''$. This resulted in the SWS apertures being offset from the nebular centre by 1.8 arcsec north in declination and by 13.6 arcsec (=1.68 sec) east in right ascension, giving a total offset of 13.8 arcsec from the centre of the nebula. The effects of this SWS aperture offset, together with the particular spacecraft roll angle at the time of the observations (retrieved from the *ISO* archives) and the SWS subspectra beam profiles, are sufficient largely to explain the discrepancies initially found between the model predictions and the observations. The wavelength-dependent aperture sizes of the *ISO* SWS range from 14 × 20 arcsec^2 for 2.38 μm $\leqslant \lambda \leqslant$ 12.0 μm, 14 × 27 arcsec^2 for 12.0 μm $\leqslant \lambda \leqslant$ 27.5 μm, 20 × 27 arcsec^2 for 27.5 μm $\leqslant \lambda \leqslant$ 29.0 μm, to 20 × 33 arcsec^2 for 29.0 μm $\leqslant \lambda \leqslant$ 45.2 μm (de Graaw et al. 1996). Five of the six infrared fine-structure lines listed in Table 15 were observed by the *ISO* SWS through a 14 × 27 arcsec^2 aperture, while the [S IV] 10.5 μm line was observed through a 14 × 20 arcsec^2 aperture. As mentioned above, the aperture dimensions are not the only factor to be taken into account – there is also the transmission efficiency profile across the spatial aperture, which, in some cases, is far from flat (Leech et al. 2002).

This paper has been typeset from a TEX/LATEX file prepared by the author.